

Official Journal of Turkish Society of Magnetic Resonance

CRMRI

Current Research in MRI

Comparison of Volume Measurements on Magnetic Resonance Imaging and Cadaveric Sections of the Lentiform Nucleus and Its Importance in Functional Neurosurgery Procedures

Selim Kayacı, Fatma Beyazal Çeliker, Orhan Baş, Semih Diyarbakır, Mehmet Faik Özveren

Breast Imaging with Diffusion-Weighted Magnetic Resonance Imaging: Evaluating Apparent Diffusion Coefficient Values and Biomarker Expression in Benign and Malignant Lesions

Düzgün Can Şenbil, Esra Bilici, Taner Kösetürk, Türkhun Çetin

Magnetic Resonance Imaging Examination for the Detection of Cranial Complications in Pediatric Patients with Post-Coronavirus Disease 2019 Infection

Ömer Kazcı

Ratio of Incidentally Detected Brain Tumors in Diffusion Magnetic Resonance Imaging Scans Performed in the Emergency Department on the Suspicion of Acute Stroke

Eren Tobcu, Erdal Karavaş, Özlem Çelik Aydın, Bilgin Topçu

The Role of Multiparametric Scrotal Magnetic Resonance Imaging in the Histological Differentiation of Germ Cell Neoplasia In Situ-Related Testicular Germ Cell Tumors: Can Seminomatous and Mixed-Non-Seminomatous Germ Cell Tumors Be Separated?

Serdar Aslan, Uluhan Eryürük, Ural Oğuz, İsmet Miraç Çakır

Editor in Chief

Mecit Kantarcı 

Department of Radiology, Erzincan Binali Yıldırım University, Faculty of Medicine; Atatürk University, Faculty of Medicine, Erzincan, Erzurum, Turkey

Editors

Abdominal Radiology

Aytekin Oto 

The University of Chicago, Department of Radiology, Chief Physician, Head of the Faculty Practice Plan and Dean for Clinical Affairs, Chicago, USA

Murat Danacı 

Department of Radiology, Ondokuz Mayıs University, Faculty of Medicine, Samsun, Turkey

Breast Radiology

Serap Gültekin 

Department of Radiology, Gazi University, Faculty of Medicine, Ankara, Turkey

Cardiac Radiology

Memduh Dursun 

Department of Radiology, İstanbul University, İstanbul Faculty of Medicine, İstanbul, Turkey

Cihan Duran 

Department of Diagnostic and Interventional Imaging, The University of Texas, McGovern Medical School, Texas, USA

Emergency Radiology

Mehmet Ruhi Onur 

Department of Radiology, Hacettepe University Faculty of Medicine Hospital, Ankara, Turkey

Engineer Group

Esin Öztürk Işık 

Biomedical Engineering, Boğaziçi University, İstanbul, Turkey

Head & Neck Radiology

Nafi Aygün 

Department of Radiology, Johns Hopkins University School of Medicine, Baltimore, Maryland, USA

Hatice Gül Hatipoğlu 

Department of Radiology, Health Science University, Gulhane Faculty of Medicine, Ankara Bilkent City Hospital, Ankara, Turkey

Musculoskeletal Radiology

Nil Tokgöz 

Department of Radiology, Gazi University, Faculty of Medicine, Ankara, Turkey

Neuroradiology Radiology


Alpay Alkan 

Department of Radiology, Bezmialem Vakıf University, Faculty of Medicine, İstanbul, Turkey

Pediatric Radiology

Korgün Koral 

Department of Radiology, University of Texas Southwestern Medical Center, Dallas, TX, USA

Süreyya Burcu Görkem 

Department of Pediatric Radiology, Adana State Hospital, Adana, Turkey

Thorax Radiology

Polat Koşucu 

Department of Radiology, Karadeniz Teknik University, Faculty of Medicine, Trabzon, Turkey

Biostatistical Consultant

Sonay Aydın 

Department of Radiology, Erzincan Binali Yıldırım University, Faculty of Medicine, Erzincan, Turkey



Founder

İbrahim KARA

General Manager

Ali ŞAHİN

Finance Coordinator

Elif YILDIZ ÇELİK

Journal Managers

Deniz KAYA

İrmak BERBEROĞLU

Arzu ARI

Publications Coordinators

Gökhan ÇİMEN

Alara ERGİN

İrem ÖZMEN

Derya AZER

Beril TEKAY

Nisanur ATICI

Project Coordinators

Doğan ORUÇ

Sinem Fehime KOZ

Contact

Address: Büyükdere Cad. 199/6 34394

Mecidiyeköy, Şişli, İstanbul, Turkey

Phone: +90 212 217 17 00

E-mail: info@avesyayincilik.com

About the Current Research in MRI

Current Research in MRI is a peer reviewed, open access, on-line-only journal published by the Turkish Society of Magnetic Resonance.

Current Research in MRI is a triannual journal that is published in English in April, August, and December.

Indexing

Current Research in MRI is covered in the following indexing database;

- EBSCO

All content published in the journal is permanently archived in Portico.

Aims, Scope, and Audience

Current Research in MRI aims to publish studies of the highest scientific and clinical value. It also encourages the submission of high-quality research in the field of radiology.

Current Research in MRI covers a wide range of topics related to radiology.

Current Research in MRI publishes original articles, reviews, case reports, and letters to the editor that are prepared in accordance with ethical guidelines.

The target audience of the journal includes healthcare professionals, physicians, and researchers who are interested in or working in the field of radiology.

You can reach the current version of the instructions to authors at <https://curremr.com/EN>

Editor in Chief: Mecit Kantarcı

Address: Department of Radiology, Erzincan Binali Yıldırım University School of Medicine, Erzincan, Turkey

E-mail: akkanrad@hotmail.com

Publisher: Turkish Society of Magnetic Resonance

Address: Konak Mah. 858. Sok. No: 2 Çakıroğlu İş Hanı Kat: 5
Daire: 55 Konak / İzmir, Turkey

Publishing Services: AVES

Address: Büyükdere Cad., 199/6 34394 Şişli, İstanbul, Turkey

Phone: +90 212 217 17 00

E-mail: info@avesyayincilik.com

Webpage: www.avesyayincilik.com

CONTENTS

ORIGINAL ARTICLES

- 41** Comparison of Volume Measurements on Magnetic Resonance Imaging and Cadaveric Sections of the Lentiform Nucleus and Its Importance in Functional Neurosurgery Procedures
Selim Kayacı, Fatma Beyazal Çeliker, Orhan Baş, Semih Diyarbakır, Mehmet Faik Özveren
- 50** Breast Imaging with Diffusion-Weighted Magnetic Resonance Imaging: Evaluating Apparent Diffusion Coefficient Values and Biomarker Expression in Benign and Malignant Lesions
Düzgün Can Şenbil, Esra Bilici, Taner Kösetürk, Türkhun Çetin
- 55** Magnetic Resonance Imaging Examination for the Detection of Cranial Complications in Pediatric Patients with Post-Coronavirus Disease 2019 Infection
Ömer Kazcı
- 59** Ratio of Incidentally Detected Brain Tumors in Diffusion Magnetic Resonance Imaging Scans Performed in the Emergency Department on the Suspicion of Acute Stroke
Eren Tobcu, Erdal Karavaş, Özlem Çelik Aydın, Bilgin Topçu
- 63** The Role of Multiparametric Scrotal Magnetic Resonance Imaging in the Histological Differentiation of Germ Cell Neoplasia In Situ-Related Testicular Germ Cell Tumors: Can Seminomatous and Mixed-Non-Seminomatous Germ Cell Tumors Be Separated?
Serdar Aslan, Uluhan Eryürük, Ural Oğuz, İsmet Miraç Çakır

LETTER TO THE EDITOR

- 70** Spontaneous Intracystic and Subdural Hemorrhage of an Arachnoid Cyst: A Case Report with Baseline Imaging of an Intact Cyst
Muhsin Özgün Öztürk, Zeynep Betül Deve

REVIEWER LIST

- 72** Acknowledgement of Reviewers

Comparison of Volume Measurements on Magnetic Resonance Imaging and Cadaveric Sections of the Lentiform Nucleus and Its Importance in Functional Neurosurgery Procedures

Selim Kayacı¹, Fatma Beyazal Çeliker², Orhan Baş³, Semih Diyarbakır⁴, Mehmet Faik Özveren⁵

¹Department of Neurosurgery, Erzincan Binali Yıldırım University, Faculty of Medicine, Erzincan, Turkey

²Department of Radiology, Recep Tayyip Erdoğan University, Faculty of Medicine, Rize, Turkey

³Department of Anatomy, Samsun University, Faculty of Medicine, Samsun, Turkey

⁴Department of Anatomy, Erzincan Binali Yıldırım University, Faculty of Medicine, Erzincan, Turkey

⁵Department of Neurosurgery, Anadolu Hospital, Kütahya, Turkey

Cite this article as: Kayacı S, Beyazal Çeliker F, Baş O, Diyarbakır S, Özveren MF. Comparison of volume measurements on magnetic resonance imaging and cadaveric sections of the lentiform nucleus and its importance in the functional neurosurgery procedures. *Current Research in MRI* 2023;2(3):41-49.

Corresponding author: Selim Kayacı, e-mail: selim_kayaci@hotmail.com

Received: July 24, 2023 **Accepted:** September 03, 2023 **Publication Date:** October 10, 2023

DOI:10.5152/CurrResMRI.2023.23066



Content of this journal is licensed under a Creative Commons Attribution-NonCommercial 4.0 International License.

ABSTRACT

Objective: Functional neurosurgery is one of the fastest-growing areas of neurosurgery. However, complications are encountered that are not negligible during the operations. In this study, we measure and compare the volume of the lentiform nucleus using magnetic resonance imaging (MRI) and anatomical sections.

Methods: Thirteen adult brain cadavers were used in this study. First, 2-mm-thick MRI sections were obtained, and the volume of the lentiform nuclei was measured on the obtained images. Then, agar-embedded brain specimens were cut into 4-mm-thick coronal sections using a microtome. The sections were scanned, and the volume of the lentiform nuclei was calculated using image processing software. The MRI-based and anatomical section-based metrics were compared.

Results: The mean right and left lentiform nucleus volumes on MRI were $5821.4 \pm 590.5 \text{ mm}^3$ and $5781.8 \pm 723.5 \text{ mm}^3$, respectively. The corresponding mean volumes calculated from the cadaveric sections were $5503.4 \pm 595.5 \text{ mm}^3$ and $5332.3 \pm 599.7 \text{ mm}^3$, respectively. There was no significant difference between the volume calculated from MRI and that obtained from the cadaveric section ($P < .001$). On MRI, the volumes of the right and left lentiform nuclei were not significantly different ($P = .681$). Similarly, the volumes of the right and left lentiform nuclei measured from cadaveric sections were not significantly different ($P = .069$).

Conclusion: This study showed a correlation between the measurement of the lentiform nucleus volume based on MRI and that calculated from anatomical sections. Our findings support the reliability of using MRI for stereotactic functional neurosurgical procedures.

Keywords: Anatomy, functional neurosurgery, lentiform nucleus, magnetic resonance imaging, stereology

INTRODUCTION

The lentiform nucleus (also referred to as the nucleus lentiformis) is a large, cone-shaped mass of gray matter that forms the central nucleus of the cerebral hemisphere, the convex base of which consists of the putamen and the apical part of the globus pallidus. The lentiform nucleus is divided into two parts. The inner part is called the globus pallidus, and the outer part is called the putamen. Globus pallidus appears lighter than the putamen because it contains a large amount of myelinated nerve fibers. The lentiform nucleus is bounded by the anterior limb of the internal capsule from the caudate nucleus and the posterior limb of the internal capsule from the thalamus.¹ The putamen is believed to play an additional role in memory formation, specifically muscle memory. For example, activities such as learning to ride a bicycle involve the use of putaminal nuclei. Globus pallidus, on the other hand, is involved in the execution of fine movements and preventing abnormal movements.¹

The putamen and globus pallidus are more enriched in mitochondria, vascular nutrition, neurotransmitters, and chemical content compared to the other areas of the brain. Therefore, these have higher metabolic activity, leading to a higher rate of utilization of glucose and oxygen. Due to this feature, the lentiform nucleus is more vulnerable to systemic and metabolic disorders.²

Pathologies affecting the putamen and globus pallidum can lead to Parkinson's disease (PD) and other movement disorders. It is relatively easy to describe the clinical manifestations of the involvement of the internal capsule. However, it is relatively difficult to distinguish the patterns of clinical presentation resulting from the involvement of the putamen and globus pallidus.³ Girround et al described two clinical syndromes occurring due to brain involvement limited to the lentiform nucleus: (i) behavioral disorder due to infarction of the globus pallidus and cognitive function

disorders and (ii) motor (dystonia) and cognitive dysfunction due to the involvement of the putamen.⁴ Bhatia and Marsden published a series of 240 patients with focal lesions in the basal ganglia. Dystonia and abulia (loss of the ability to make conscious decisions and move) were found to be the most common motor abnormalities with lentiform and caudate nuclei lesions in this investigation. Other behavioral problems are also common in lesions of the specified nucleus.⁵

Similarly, concomitant involvement of the putamen, caudate nucleus, thalamus, and parietal cortex may cause acute and subacute posthemiplegic focal dystonia or hemidystonia.⁶ However, in most cases, the involvement of the internal capsule is due to the enlargement of the lesion, which affects the neighboring structures. Other motor disorders such as unilateral chorea,⁷ hemichorea–hemiballismus, asterixis- acute motor stereotypes,⁸ acute focal dystonias, and subacute parkinsonism,⁹ have been reported after unilateral lesions of the lentiform nucleus. Globus pallidus lesions can cause behavioral and speech disorders. In most cases, motor disturbances may occur several months or years after the onset of the acute lesion.⁴

According to the published literature, putaminal lesions typically occur after head trauma. Ischemic stroke due to pure lesions of the putamen has rarely been reported.⁴ Putaminal infarct usually progresses to adjacent tissues, creating a wider clinical picture.⁴

Apart from ischemic or hemorrhagic strokes and trauma, some neurodegenerative diseases can cause serious neurological pictures by affecting the basal nuclei. Among these, the best known are Wilson's disease,¹⁰ Hallervorden–Spatz disease,¹¹ and Fahr's syndrome.¹²

Radiological methods are used for the diagnosis of both ischemic and hemorrhagic strokes as well as post-traumatic lesions in the brain, including basal nuclei. Although computed tomography is a practical and inexpensive method, it may not adequately demonstrate the changes in brain tissue, especially ischemic changes. Magnetic resonance imaging (MRI) is much more sensitive to brain parenchymal changes and is superior in terms of showing tissue-level changes.

Stereotactic surgery is an important minimally invasive neurosurgical method. It involves the localization of anatomical targets in the brain using an external, three-dimensional (3D) reference system. Stereotactic surgery allows access to deep-seated and small lesions without extensive craniotomy and damage to normal brain tissue. The value of stereotactic biopsy in neuro-oncology is undisputed, as it

enables sampling of the required tissue without damaging the normal tissues, enabling accurate diagnosis and treatment. Although there are nuanced differences in the applied systems, the main underlying principle is always the same, i.e., accessing the target tissue by stereotactic methods based on geometric planning using radiological imaging (without direct visual access).

However, there are some pertinent unresolved issues related to the localization of the basal nuclei with stereotactic methods using cranial MRI. To what extent is it possible to accurately detect these target tissues anatomically? To understand this, it is instructive to compare the morphometric measurements of basal nuclei in cadaveric specimens with the morphometric measurements made in cranial MR images.

Functional neurosurgery and deep brain stimulation (DBS) are probably one of the fastest-growing areas of neurosurgery. Although these procedures (ablative or nonablative) are minimally invasive, they have many complications and side effects, such as infection, system malfunction, intracerebral hemorrhage, skull fracture, skin erosion, and foreign body reaction.¹³⁻¹⁷ Among these complications, the inability to properly place the system (malposition) is related to the inability to accurately localize the target anatomical point. Therefore, in this study, we calculated and compared the volumes of lentiform nuclei stereologically by making radiological and then anatomical sections in cadaveric specimens and evaluated the results in terms of functional neurosurgical procedures.

Many published studies have measured brain basal nuclei volumes using MRI or CT. In most of these studies, volume changes in basal nuclei were performed for comparison in some disease states.¹⁸⁻²¹ However, there are no in-depth studies involving the calculation of the lentiform nucleus volume in cadaver samples. In particular, we could not find any study that compared lentiform nucleus volumes by measuring them first in MRI and then in cadaver samples and emphasizing the importance of this in terms of functional neurosurgical procedures. In this respect, we believe that our study makes an important contribution to contemporary literature.

Purpose: To measure and compare the volume of the lentiform nucleus using MRI and the anatomical sections.

METHODS

This study was approved by the Clinical Ethics Committee of Recep Tayyip Erdoğan University (approval no. 2022/173, dated October 6, 2022). The study was conducted using brain specimens removed by autopsy from 15 adult human cadavers. The age, sex, and disease status of the cadavers were unknown. These cadaver specimens were approximately 10 years old and were fixed in 10% formaldehyde. Two of the cadaver samples were excluded from the study because they were not of suitable quality. For the remaining 13 cadaver specimens, firstly, MRI images were obtained (section thickness: 2 mm; intervals of 1 mm) (Figure 1). These specimens were then embedded in agar. Then, 4 mm-thick sections were prepared with a microtome.

Magnetic Resonance Imaging Procedure

Imaging of the cadavers was performed using a 36-channel 1.5T MRI device (Discovery MR 750w, GEM-70, General Electric Company, USA). Turbo spin echo (T1 FLAIR) images with a section thickness of 2 mm were obtained in the coronal plane using a head coil (Figure 2). Imaging parameters were as follows: repetition time (TR): 2310; time to echo (TE): 8.1/Ef, EC: 1/135.7 kHz; inversion time (TI): 974; Head

MAIN POINTS

- Functional neurosurgery is one of the fastest growing areas of neurosurgery. However, complications are encountered which are not negligible during the operations.
- Among these complications, the inability to place the system properly (malposition) is related to the inability to accurately localize the target anatomical point.
- Therefore, in this study, we calculated and compared the volumes of lentiform nuclei stereologically by first making radiological and then anatomical sections in cadaveric specimens.
- This study shows a correlation between measurement of lentiform nucleus volume based on MRI and those calculated from anatomical sections. Our findings support the reliability of functional neurosurgical procedures using MRI and stereotactic method.

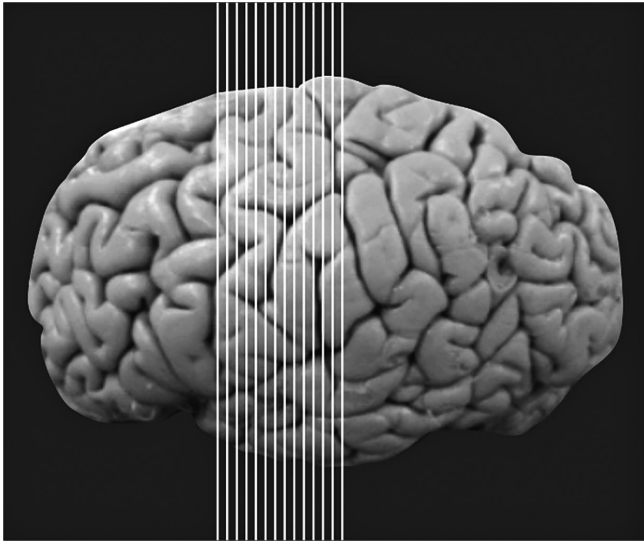


Figure 1. Obtaining TSE (T1 FLAIR) images with a section thickness of 2 mm by skipping 1 cm by segmentation method on coronal plane MRI. FLAIR, fluid-attenuated inversion recovery; MRI, magnetic resonance imaging; TSE, turbo spin echo.

24/FL: a; field-of-view (FOV): 24×21.6 , 2.00 thk/1.00 sp, 60/06:25, and $320 \times 224/2.00$ number of excitations (NEX). The number of sections on which the lentiform nucleus appeared on MR images was calculated. Onis 2.5 [Onis Free Edition 2.5 Download—Onis.exe] and Image J (<https://imagej.net/Downloads>) software were then used to calculate the lentiform nucleus volume from the MR images. Onis 2.5 is an analytical program that rapidly converts images into DICOM format serially (Figure 3). Image J software is used for image analysis, processing, and surface area calculation in clinical and scientific studies (Figure 4).

Preparation of Cadaver Specimens

Agar (Trypticase Soy Agar, Merck) was prepared for the detection of the samples. For this process, 1.5% powdered agar was mixed in distilled water to prepare a solution. The solution was dissolved in a boiling water bath. Subsequently, it was sterilized in an autoclave at 121°C and then cooled to 50°C . The samples were placed in plastic boxes. The agar was poured so that it overflowed 2 cm at the edges of the samples. It was left to freeze for 6 hours at room temperature. A Bosch MAS9454M bslicing machine was used for cutting the cadaver specimens. Then, 4 mm-thick coronal sections were prepared (Figure 5). Sections thinner than 4 mm could not be obtained because they led to sample fragmentation. The obtained sections were scanned

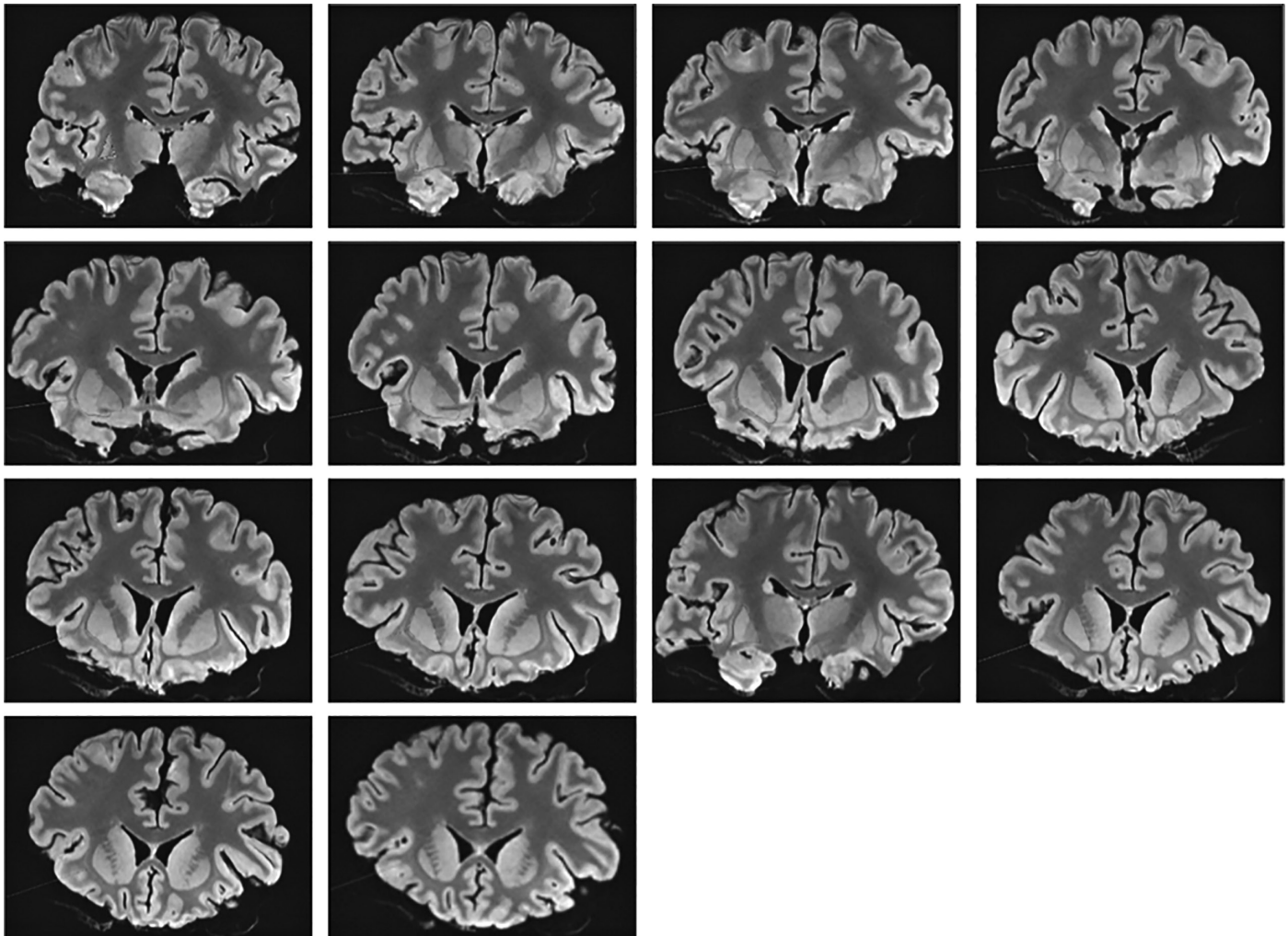


Figure 2. Sections in which lentiform nuclei are seen in the frontal plane in a sample cadaver on MRI. MRI, magnetic resonance imaging.



Figure 3. Evaluation of MR image in Onis 2.5 analysis program. MR, magnetic resonance.

using a scanner (Xerox, Workcentre 7428, USA), and the images were uploaded to a desktop computer (HP, ProDesk 600, G2, MT, USA) (Figure 6). The total number of sections obtained from each cadaver and the number of sections with lentiform nuclei were noted (Table 1). The Image J image program was used to set the scale and calculate the surface area on these images (Figure 7).

Calculation of Volume According to the Cavalieri Principle

The volumes of the lentiform nuclei were calculated using the Cavalieri principle and the planimetry technique on MRIs and cadaver cross-sectional images. For volume calculations, the surface areas of the lentiform nuclei on the MRIs converted to Cadaver and DICOM formats

were calculated by the planimetry method using the Image J program (Figure 4). Each measurement was performed in a blinded fashion by the same researcher at least three times, and the average values were taken. The volumes of the lentiform nuclei were calculated by entering the sum of the surface areas in the following formula, based on the literature.^{22,23}

$$V = t \times \sum A$$

where t represents the thickness of the successive sections and $\sum A$ represents the total surface area of the thalamus found in the section

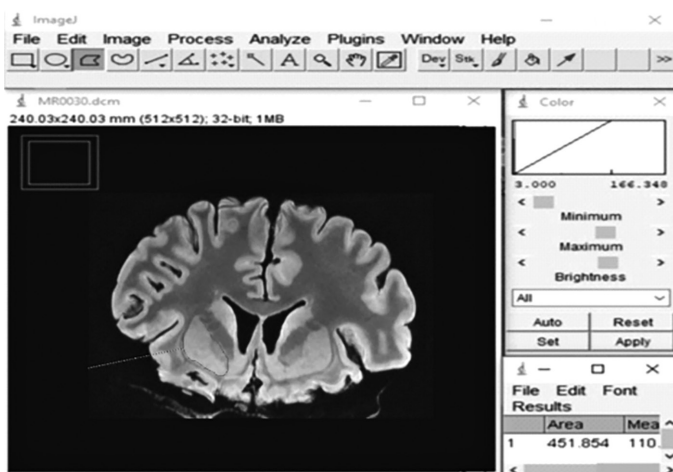


Figure 4. Evaluation of MR image in J image analysis program. MR, magnetic resonance.

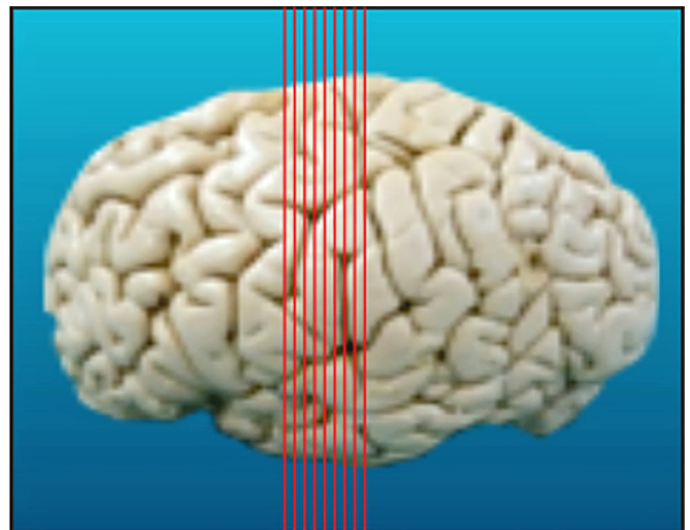


Figure 5. Sectioning 4 mm thick in a cadaver sample.

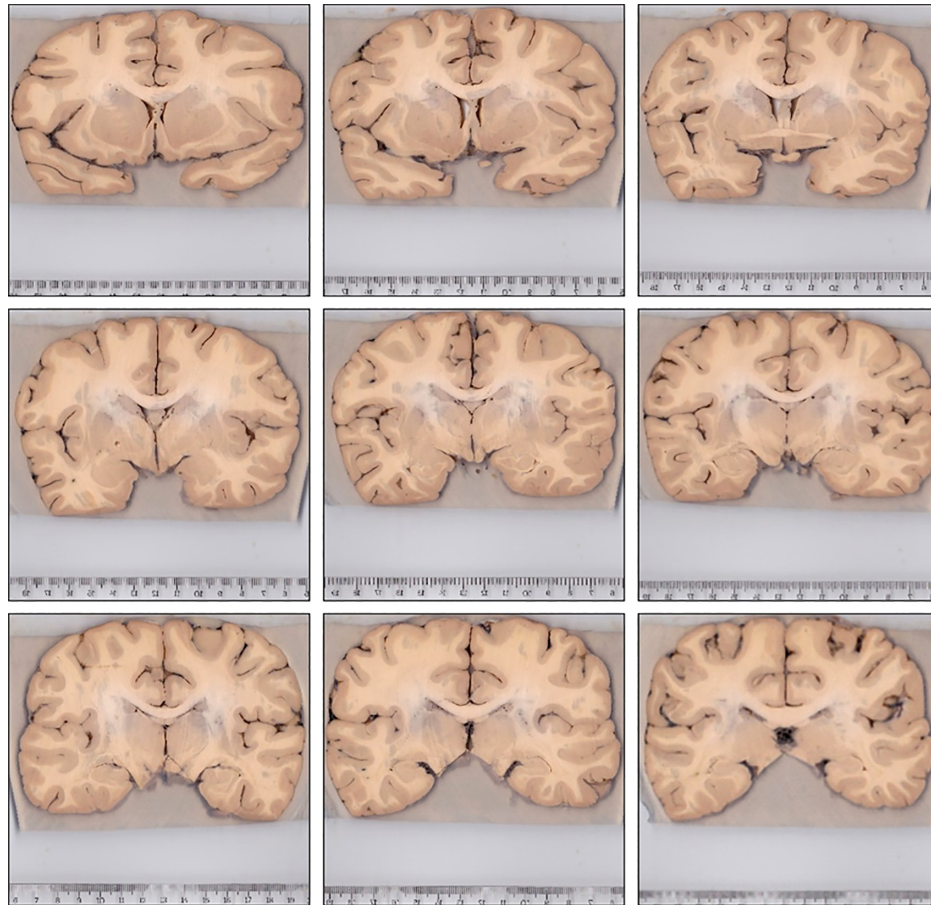


Figure 6. The appearance of lentiform nuclei for the fifth cadaver on coronal plane.

images. All data were entered into a pre-prepared Microsoft Excel spreadsheet containing the above formula, and the calculation was

automatically performed. The volumes of the lentiform nuclei in each cerebral hemisphere were calculated separately.

Table 1. Sections Numbers of MRI and Cadaveric Specimens (n=13)

Cadaver No.	The Total Section Number on MRI	The Total Section Number on Cadaver	The Number of Sections of the Right Lentiform Nucleus on MR	The Number of Sections of the Left Lentiform Nucleus on MR	The Number of Sections of the Right Lentiform Nucleus on Cadaver	The Number of Sections of the Left Lentiform Nucleus on Cadaver
1	58	42	14	13	9	9
2	56	38	12	13	8	8
3	55	38	14	13	8	9
4	51	36	11	11	7	7
5	52	37	12	13	9	9
6	54	36	12	12	7	8
7	52	35	11	11	7	7
8	50	36	12	13	6	7
9	59	39	15	15	8	9
10	60	36	14	14	9	10
11	45	37	12	13	8	8
12	60	37	14	15	8	7
13	58	41	13	12	9	9
Mean	54.61	37.53	12.69	12.92	7.84	8.23
Minimum-maximum	45-60	36-42	11-15	11-15	6-9	7-10
Total number	710	488	166	168	103	107

MRI, magnetic resonance imaging; n, number of cadavers.

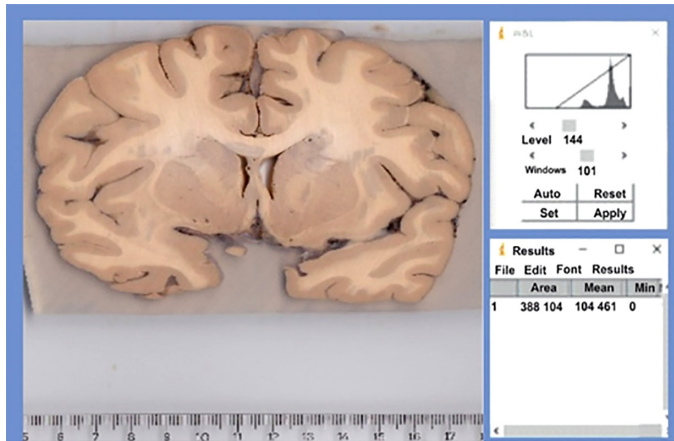


Figure 7. Calculation of the surface area of lentiform nuclei in cadaveric sections with image J program.

Statistical Analysis

Results are presented as mean \pm standard deviation, or median (max-min) for continuous variables. Comparisons between right- and left-sided measurements were made using the paired *t*-test. First, the relationship between MRI, and cadaver measurements was examined using the Pearson correlation coefficient, and the results were presented as $r(P)$. Then, reliability analysis was performed using a two-way mixed effects model in which human effects were considered random and measurement effects were fixed. The model was used to calculate the Absolute Agreement Intra-Class Correlation Coefficient (ICC). *P* values $< .05$ were considered statistically significant. Statistical analyses were performed using IBM SPSS v 19 software (IBM Software, NY, USA).

RESULTS

The total number of MRI and anatomical sections of each cadaver and the number of sections in which the lentiform nuclei were seen are shown in Table 1. In MRI, the total number of cadaver sections was 710; the mean number of sections was 54.61 (range: 45-60); the total

Table 3. Volume of the Lentiform Nuclei with Different Measurement Techniques (MRI and Cadaveric Section)

Measurement Technique	Cadaveric Section	MRI	$r(p)^{**}$
Right lentiform nucleus	5503.4 \pm 595.5 5504.0 (4336.0-6532.0)	5821.4 \pm 590.5 6019.0 (4820.0-6755.0)	.95 ($<.001$)
Left lentiform nucleus	5332.3 \pm 599.7 5212.0 (3940.0-6444.0)	5781.8 \pm 723.5 5745.0 (4232.0-7064.0)	.89 ($<.001$)
<i>P</i> *	.069	.681	

MRI, magnetic resonance imaging.

*Paired samples test for right and left. **Correlation between cadaver and MRI sections.

number of sections with the right lentiform nuclei was 166; the average was 12.69 (range: 11-15); and the total number of sections with the left lentiform nuclei was 168; the mean was 12.92 (range: 11-15). The total number of sections obtained from cadaver specimens was 488, mean 37.53 (range: 36-42); the total number of sections with the right lentiform nuclei was 103, mean 7.84 (range: 6-9). The total number of sections with the left lentiform nuclei was 107, mean 8.23 (range: 7-10). The mean volumes of the right and left lentiform nuclei on MRI were 5821.4 \pm 590.5 mm³ (range: 4820-6755) and 5781.8 \pm 723.5 mm³ (range: 4232-7064), respectively. In cadaveric specimens, the right, and the left lentiform nucleus volumes were 5503.4 \pm 595.5 mm³ (range: 4336-6532) and 5332.3 \pm 599.7 mm³ (range: 3940-6444), respectively (Table 2). For the right lentiform nucleus, there was a statistically significant agreement between the two measurement techniques ($P < .001$; ICC $\rho = 0.619$). Similarly, for the left lentiform nucleus, the agreement between the two measurement techniques was statistically significant ($P < .001$; ICC $\rho = 0.714$) (Table 3).

DISCUSSION

In this study, we measured the lentiform nucleus volumes in coronal sections of 13 human cadaver brains using a 1.5T MRI device. Then, the lentiform nucleus volumes were measured in the anatomical coronal sections of the same cadaver samples using a microtome. The results obtained with the 2 methods were compared, and the importance of these results in terms of functional neurosurgical procedures was investigated.

Table 2. MRI and Cadaver Lentiform Nucleus Volumes (mm³) (n=13)

Cadaver No.	MRI		Cadaver Sections	
	Right	Left	Right	Left
1	5605.0	5413.0	5396.0	5040.0
2	5279.0	5362.0	4824.0	5212.0
3	6755.0	6692.0	6532.0	6444.0
4	6053.0	5745.0	5924.0	5532.0
5	4872.0	5132.0	4828.0	4976.0
6	6019.0	5553.0	5420.0	5164.0
7	5969.0	5581.0	5844.0	5100.0
8	6034.0	6062.0	5632.0	5684.0
9	6288.0	6408.0	5908.0	6004.0
10	4820.0	4232.0	4336.0	3940.0
11	6516.0	7064.0	6116.0	5644.0
12	6044.0	6108.0	5504.0	5532.0
13	5424.0	5812.0	5280.0	5048.0
Mean \pm SD	5821.4 \pm 590.5	5781.8 \pm 723.5	5503.4 \pm 595.5	5332.3 \pm 599.7
Median	6019.0	5745.0	5504.0	5212.0
Minimum-maximum	4820.0-6755.0	4232.0-7064.0	4336.0-6536.0	3940.0-6444.0

MRI, magnetic resonance imaging; n, number of cadavers.

Understanding the brain structures in 3D and performing volumetric measurements is of great importance for the correct diagnosis and treatment of brain diseases. Two-dimensional tools (for example, anatomy books) or traditional 3D tools (e.g., plastic models) are not sufficient to understand the 3D structures of the brain. For this purpose, the availability of high-resolution MRI methods is important. MRI-based volume measurement is now increasingly used to investigate neuro-anatomical structures in patients with neurological and psychiatric disorders such as PD, schizophrenia, Alzheimer's disease (AD), and epilepsy.²³⁻²⁵

Automated segmentation methods using MRI have been described in many studies. Calmon and Roberts reported a segmentation method for lateral ventricles on coronal plane MRI.²⁶ Stokking et al developed morphology-based brain segmentation using T1-weighted MRI for fully automated segmentation.²⁷ Webb et al reported an automatic partitioning method for the detection of hippocampal atrophy.²⁸ Each of these methods is based on the fragmentation of the target object in each MRI, obtained in different indexes.

Wang et al published a study of 1000 patients (age range, 18-70 years) to investigate various diseases related to the lentiform nucleus in the Chinese population. The patients were divided into 5 age groups (18-30, 31-40, 41-50, 51-60, and 61-80). Each group consisted of 100 men and 100 women. All volunteers underwent MRI examination using a T1-weighted 3D magnetization-prepared rapid acquisition gradient echo array. The relationship of the lentiform nucleus volume with age and sex was analyzed. The mean left and right putamen volumes were $4811.59 \pm 588.99 \text{ mm}^3$ and $4763.11 \pm 587.59 \text{ mm}^3$, respectively, and the volume of the left putamen was greater than that of the right putamen. The mean left and right globus pallidus volumes were $1591.31 \pm 226.81 \text{ mm}^3$ and $1627.28 \pm 235.06 \text{ mm}^3$, respectively, and the right globus pallidus volume was larger. The mean volumes of the left and right putamen and left and right globus pallidus in men were $4962.72 \pm 598.49 \text{ mm}^3$, $4909.83 \pm 600.54 \text{ mm}^3$, $1623.24 \pm 234.16 \text{ mm}^3$, and $1663.18 \pm 243.56 \text{ mm}^3$, respectively. In women, these measurements were $4663.65 \pm 540.49 \text{ mm}^3$, $4619.28 \pm 537.59 \text{ mm}^3$, $1560.00 \pm 215.04 \text{ mm}^3$, and $1592.09 \pm 221.06 \text{ mm}^3$, respectively. The putamen and globus pallidus volumes were larger in men. The volumes of the left and right putamen, as well as the left and right globus pallidus, showed a decrease with age. The lentiform nucleus volume was found to be larger in men than in women. In addition, the lentiform nucleus volumes were found to decrease with aging.¹⁸

Ertekin et al measured and compared the lentiform nucleus volumes in healthy people and people with PD using both volumetric and semiautomatic segmentation methods. In the control group (healthy people), the mean lentiform nucleus volume calculated by the point counting method using a control object in MRI was $7.52 \pm 1.14 \text{ cm}^3$. In the PD group, the corresponding mean value was significantly smaller ($6.40 \pm 1.55 \text{ cm}^3$, $P < .05$). Based on the semiautomatic segmentation results, the mean lentiform nucleus volume in patients with PD ($6.52 \pm 1.38 \text{ cm}^3$) was also significantly smaller than that in healthy humans ($7.43 \pm 0.87 \text{ cm}^3$; $P < .05$).¹⁹

Derrek et al conducted a study enrolling 706 patients with AD and 639 young healthy volunteers to investigate the relationship between the lentiform nucleus volume and genome-wide. They measured the volume by taking 58 images with the segmentation method in a 1.5T MRI. In patients with AD, the lentiform nucleus volume was $6422.2 \pm 723.9 \text{ mm}^3$ on the left and $6450.9 \pm 686.9 \text{ mm}^3$ on the right, and they found a

strong correlation between the two. In healthy young people, the corresponding volume measurements were $6554.4 \pm 744.8 \text{ mm}^3$ on the left and $6729.5 \pm 765.4 \text{ mm}^3$ on the right, with a strong correlation between the left and right lentiform nucleus volumes. Although the lentiform nuclei of patients with AD were smaller than those of healthy individuals, the difference was not statistically significant.²⁰

In his doctoral thesis, Ekiz compared the volume ratio of the basal nuclei to the whole brain on the left and right sides in individuals aged 20-40 years. The mean volumes of the right and left globus pallidus in women were $1471 \pm 161.7 \text{ mm}^3$ and $1447.4 \pm 157.7 \text{ mm}^3$, respectively. The corresponding values in men were $1611.1 \pm 119.0 \text{ mm}^3$ and $1571.7 \pm 120.4 \text{ mm}^3$, respectively. The right and left putamen volumes in women were $4056.0 \pm 328.5 \text{ mm}^3$ and $4343 \pm 417.1 \text{ mm}^3$, respectively. The corresponding values in men were $4504 \pm 278.9 \text{ mm}^3$ and $4817.5 \pm 380.0 \text{ mm}^3$, respectively.²¹

The main aim of the present study was to compare the total volume measurement values in MRI sections with those obtained with anatomical sections of cadaver samples prepared using a microtome. The mean lentiform nucleus volume measurements on MRI were $5821.4 \pm 590.5 \text{ mm}^3$ on the right and $5781.8 \pm 723.5 \text{ mm}^3$ on the left. The corresponding measurements in cadaveric specimens were $5503.4 \pm 595.5 \text{ mm}^3$ and $5332.3 \pm 599.7 \text{ mm}^3$, respectively (Table 2). On comparing the measurements in MRI and cadaver samples, there was no significant difference between the right and left lentiform nucleus volumes, and there was a significant correlation between the two sides in this respect (Table 3).

Comparing the MRI-based volume measurements, these values are smaller than the values reported by Wang, Ertekin, Derrek, and Ekiz. This is likely attributable to the shrinking of the cadaver samples due to their storage in formaldehyde for 10 years, as seen in previous studies.²⁹

Since information regarding the cadaver samples' age, race, and disease status was not available, it was impossible to make comparisons as in the previous studies. In any case, the purpose of our study was not to make comparisons between age, sex, and diseased and healthy groups.

On reviewing the literature, we found a comprehensive study that measured and compared the volumes of the thalamus by first using the segmentation technique in MRI and then making sections on cadavers using the planimetry technique.³⁰ However, we did not find a similar in-depth study involving the lentiform nucleus volume measurements in cadaver samples. Only Sürücü et al measured the dimensions of the lentiform nucleus in the horizontal and coronal planes in 3D CT in a human cadaveric brain but did not calculate the volume values.³¹ Chung et al measured the dimensions of the lentiform nucleus in the horizontal and coronal planes at 0.04 mm intervals in a female cadaveric brain with 3T MRI and diffusion tensor MRI methods, but they did not measure volume either.³²

In this study, the number of 2-mm sections obtained on MRI was higher than the number of anatomical sections obtained using a microtome. This was due to section fragmentation while attempting to prepare 2-mm-thick sections in cadaver samples with a microtome. Therefore, we prepared 4-mm-thick sections. The total number of sections on MRI was 710; the total number of sections showing the lentiform nucleus was 166 on the right side and 168 on the left side (Table 1). The total number of sections obtained by cutting cadaver specimens with a

microtome was 488; the total number of sections showing the lentiform nucleus was 103 on the right and 107 on the left (Table 1). There was no significant difference between the right and left sides with respect to the number of sections obtained with the MRI and microtome. The anatomical and functional asymmetry between the right and left hemispheres of the human brain is well documented. This asymmetry has been reported between the volumes of the right and left basal nuclei.³³ In addition, there may be measurement differences due to differences in the position of cadavers during MRI and superimposition during imaging.²⁶

Various stereological methods have been developed for the volumetric analysis of structures in the cadaveric brain. The Cavalieri method is one of the most reliable and frequently used methods. It is a highly sensitive and unbiased method for quantitative measurements.^{34,35} In this method, parallel and equal-thickness portions of a body are taken, and the volume is calculated based on the total number of cross-sectional areas and the section thickness. Computed tomography, MRI, or ultrasonography cross-sectional imaging can be used to calculate the volume of an object using the Cavalieri principle.²³ Due to these properties, the Cavalieri method was used for volumetric measurements of cadaver samples in this study. In this study, 13 adult cadaver brain samples were examined. The samples were segmented on 1.5T MR devices, and after measuring the lentiform nucleus volumes, cadaver sections were prepared, and the lentiform nucleus volumes were compared stereologically.

Importance of This Study

Functional neurosurgical procedures, including ablative procedures and nonablative procedures (such as DBS), have many complications and side effects. These can be classified into 5 main groups: (i) Relatively rare natural side effects that may develop after the application of the system. These include unresponsiveness to DBS, stimulation-induced dyskinesia and dystonia, speech disorder, axial symptoms (gait disturbance, festination, freezing), ocular disorders (ocular deviation and eye opening apraxia), and psychiatric disorders (depression, anxiety, apathy, aggressive behavior, manic episodes, and impulse control disorder). (ii) Natural complications of the surgical procedure. These include infection, system malfunction, intracerebral hemorrhage, skull fracture, skin erosion, and foreign body reactions.¹³⁻¹⁷ (iii) Complications due to the surgical technique applied and the inadequacy of the system (electrode breakage, etc.). These are related to the experience or working methods of the surgical center.¹⁴ (iv) Factors related to the operator's skill and experience: e.g., system malposition resulting in the inability to accurately localize the target anatomical point. (v) Wrong patient selection. These interventional methods are applied to patients who are resistant to medical treatment in the mid-advanced stage of the disease. Additional clinical improvement may not be observed if these interventional methods are applied in the early stages and in patients who respond positively to medical treatment. Among these complications, the inability to place the system properly prevents the accurate localization of the target point. From this perspective, our results are important.

Study Limitations

Some limitations of this study should be considered while interpreting the results: (i) The age and sex of the cadaver specimens were unknown. However, this was not a significant handicap, considering the purpose of this study. (ii) The history of any ischemic, traumatic, or neurodegenerative disease in the cadaver samples was not available.

(iii) The samples used were not fresh cadaver samples. After the post-mortem examination, the cadavers were stored in formaldehyde for 10 years. This may have led to a progressive shrinking of samples over time, resulting in relatively smaller measurement values. However, the volume measurements obtained in previous studies using MRI were not significantly different from those in this study. (iv) Attempts to prepare 3-mm-thick sections with a microtome led to section fragmentation. Therefore, 4 mm-thick anatomical sections were prepared, while the MRI sections were 4 mm thick. Although this did not affect the total volume values of the lentiform nuclei, it can be seen as a limitation of this study. (v) The MRI device used in this study was 1.5 Tesla. The use of an MRI device with a higher resolution would have provided better images. For example, it would be possible to better distinguish between the putamen and the globus pallidus on a higher-resolution MRI device. However, only the 1.5T MRI device was available at our institution.

According to the results we obtained from this study, a significant correlation was found between the lentiform nucleus volumes measured using the MRI method and the volume measurements obtained by making anatomical sections. Our findings support the reliability of the DBS procedure performed using MRI with stereotactic guidance.

Ethics Committee Approval: Ethics committee approval was received for this study from the ethics committee of Recep Tayyip Erdoğan University (Date: October 6, 2022, Number: 2022/173).

Informed Consent: The cadaver specimens and MRI images used in the study were obtained from the relevant university's cadaver unit. The cadavers' names and surnames are not featured in any of the photographs. As a result, the permission form was omitted.

Peer-review: Externally peer-reviewed.

Author Contributions: Concept – S.K.; Design – S.K.; Supervision – S.K., O.B.; Resources – S.K.; Materials – S.K.; Data collection and/or Processing – S.K., F.B.Ç.; Analysis and/or Interpretation – S.K., O.B., S.D.; Literature Search – S.K., O.B.; Writing Manuscript – O.B., S.D.; Critical Review – O.B., M.F.Ö.; Other – M.F.Ö.

Declaration of Interests: The authors declare that they have no competing interest.

Funding: The authors declared that this study has received no financial support.

REFERENCES

1. Snell RS. *Clinical Neuroanatomy*. Wolters Kluwer Health/Lippincott Williams & Wilkins; 2022.
2. Hegde AN, Mohan S, Lath N, Lim CCT. Differential diagnosis for bilateral abnormalities of the basal ganglia and Thalamus. *RadioGraphics*. 2011;31(1):5-30. [\[CrossRef\]](#)
3. Moulin T, Bogousslavsky J, Chopard JL, et al. Vascular ataxic hemiparesis: a reevaluation. *J Neurol Neurosurg Psychiatry*. 1995;58(4):422-427. [\[CrossRef\]](#)
4. Giroud M, Lemesle M, Madinier G, Billiar T, Dumas R. Unilateral lenticular infarcts: radiological and clinical syndromes, aetiology, and prognosis. *J Neurol Neurosurg Psychiatry*. 1997;63(5):611-615. [\[CrossRef\]](#)
5. Bhatia KP, Marsden CD. The behavioral and motor consequences of focal lesions of the basal ganglia in man. *Brain*. 1994;117(4):859-876. [\[CrossRef\]](#)
6. Marsden CD, Obeso JA, Zarranz JJ, Lang AE. The anatomical basis of symptomatic hemidystonia. *Brain*. 1985;108(2):463-483. [\[CrossRef\]](#)
7. Chang MH, Chiang HT, Lai PH, Sy CG, Lee SS, Lo YY. Putaminal petechial haemorrhage as the cause of chorea: a neuroimaging study. *J Neurol Neurosurg Psychiatry*. 1997;63(3):300-303. [\[CrossRef\]](#)
8. Maraganore DM, Lees AJ, Marsden CD. Complex stereotypies after right putaminal infarction: a case report. *Mov Disord*. 1991;6(4):358-361. [\[CrossRef\]](#)

9. Kulisevsky J, Berthier ML, Avila A, Roig C. Unilateral parkinsonism and stereotyped movements following a right lenticular infarction. *Mov Disord.* 1996;11(6):752-754. [\[CrossRef\]](#)
10. Brewer GJ. *Wilson's Disease: A Clinician's Guide to Recognition, Diagnosis, and Management.* Kluwer Academic, Boston; 2001.
11. Hogarth P, Kurian MA, Gregory A, et al. Consensus clinical management guideline for pantothenate kinase-associated neurodegeneration (PKAN). *Mol Genet Metab.* 2017;120(3):278-287. [\[CrossRef\]](#)
12. Warren JD, Mummery CJ, Al-Din AS, Brown P, Wood NW. Corticobasal degeneration syndrome with basal ganglia calcification: Fahr's disease as a corticobasal look-alike? *Mov Disord.* 2002;17(3):563-567. [\[CrossRef\]](#)
13. Constantoyannis C, Berk C, Honey CR, Mendez I, Brownstone RM. Reducing hardware-related complications of deep brain stimulation. *Can J Neurol Sci.* 2005;32(2):194-200. [\[CrossRef\]](#)
14. Hariz MI. Complications of deep brain stimulation surgery. *Mov Disord.* 2002;17(3)(suppl 3):S162-S166. [\[CrossRef\]](#)
15. Morishita T, Foote KD, Burdick AP, et al. Identification and management of deep brain stimulation intra- and postoperative urgencies and emergencies. *Parkinsonism Relat Disord.* 2010;16(3):153-162. [\[CrossRef\]](#)
16. Fenoy AJ, Simpson RK Jr. Risks of common complications in deep brain stimulation surgery: management and avoidance. *J Neurosurg.* 2014;120(1):132-139. [\[CrossRef\]](#)
17. Chan DT, Zhu XL, Yeung JH, et al. Complications of deep brain stimulation: a collective review. *Asian J Surg.* 2009;32(4):258-263. [\[CrossRef\]](#)
18. Wang GK, Chen N, Wang X, Zhuo Y. Measuring the volume of the lentiform nucleus in healthy Chinese adults based on high-resolution MRI. *Chin J Med Imaging Technol.* 2012;28(1):15-18.
19. Ertekin T, Acer N, İçer S, Vurdem ÜE, Çınar Ş, Özçelik Ö. Volume Estimation of the Subcortical Structures in Parkinson's Disease Using Magnetic Resonance Imaging: Methodological Study. *Neurol Asia.* 2015;20(2):143-153.
20. Hibar DP, Stein JL, Ryles AB, et al. Genome-wide association identifies genetic variants associated with lentiform nucleus volume in N=1345 young and elderly subjects. *Brain Imaging Behav.* 2013;7(2):102-115. [\[CrossRef\]](#)
21. Ekiz Y. *20-40 Yaş Arası Bireylerde Bazal Çekirdeklerin Hacminin Tüm Beyne Olan Hacim Oranı ve Sağ Sol Kıyaslanması Doktora tezi.* İstanbul Medipol Üniversitesi, İstanbul. 2020.
22. Şahin B, Emirzeoglu M, Uzun A, et al. Unbiased estimation of the liver volume by the Cavalieri principle using magnetic resonance images. *Eur J Radiol.* 2003;47(2):164-170. [\[CrossRef\]](#)
23. Acer N, Sahin B, Baş O, Ertekin T, Usanmaz M. Comparison of three methods for the estimation of total intracranial volume: stereologic, planimetric, and anthropometric approaches. *Ann Plast Surg.* 2007;58(1):48-53. [\[CrossRef\]](#)
24. Bas O, Acer N, Mas N, Karabekir HS, Kusbeci OY, Sahin B. Stereological evaluation of the volume and volume fraction of intracranial structures in magnetic resonance images of patients with Alzheimer's disease. *Ann Anat.* 2008;191:186-195.
25. Bernasconi N, Andermann F, Arnold DL, Bernasconi A. Entorhinal cortex MRI assessment in temporal, extratemporal, and idiopathic generalized epilepsy. *Epilepsia.* 2003;44(8):1070-1074. [\[CrossRef\]](#)
26. Calmon G, Roberts N. Automatic measurement of changes in brain volume on consecutive 3D MR images by segmentation propagation. *Magn Reson Imaging.* 2000;18(4):439-453. [\[CrossRef\]](#)
27. Stokking R, Vincken KL, Viergever MA. Automatic morphology-based brain segmentation (MBRASE) from MRI-T1 data. *Neuroimage.* 2000;12(6):726-738. [\[CrossRef\]](#)
28. Webb J, Guimond A, Eldridge P, et al. Automatic detection of hippocampal atrophy on magnetic resonance images. *Magn Reson Imaging.* 1999;17(8):1149-1161. [\[CrossRef\]](#)
29. Jonmarker S, Valdman A, Lindberg A, Hellström M, Egevad L. Tissue shrinkage after fixation with formalin injection of prostatectomy specimens. *Virchows Arch.* 2006;449(3):297-301. [\[CrossRef\]](#)
30. Kayacı S, Bas O, Celiker FB, et al. Comparison of Thalamus volume on magnetic resonance and cadaveric section images. *Turk Neurosurg.* 2020;30(4):491-500. [\[CrossRef\]](#)
31. Sürücü HS, Aldur MM, Çelik HH. Three-dimensional reconstruction of the lentiform nucleus from serial sections in man. *Folia Morphol.* 2002;61(3):153-156.
32. Chung BS, Han M, Har D, Park JS. Advanced Sectioned Images of a Cadaver Head with voxel Size of 0.04 mm. *J Korean Med Sci.* 2019;34(34):e218. [\[CrossRef\]](#)
33. Vernaleken I, Weibrich C, Siessmeier T, et al. Asymmetry in dopamine D(2/3) receptors of caudate nucleus is lost with age. *Neuroimage.* 2007;34(3):870-878. [\[CrossRef\]](#)
34. Gundersen HJ, Jensen EB. The efficiency of systematic sampling in stereology and its prediction. *J Microsc.* 1987;147(3):229-263. [\[CrossRef\]](#)
35. Mayhew TM, Gundersen HJG. 'If you assume, you can make an ass out of u and me': a decade of the disector for stereological counting of particles in 3D space. *J Anat.* 1996;188(1):1-15.

Breast Imaging with Diffusion-Weighted Magnetic Resonance Imaging: Evaluating Apparent Diffusion Coefficient Values and Biomarker Expression in Benign and Malignant Lesions

Düzgün Can Şenbil¹, Esra Bilici¹, Taner Kösetürk², Türkhun Çetin¹

¹Department of Radiology, Erzincan Binali Yıldırım University, Faculty of Medicine, Erzincan, Turkey

²Department of Anatomy, Erzincan Binali Yıldırım University, Faculty of Medicine, Erzincan, Turkey

Cite this article as: Şenbil DC, Bilici E, Kösetürk T, Çetin T. Breast imaging with diffusion-weighted magnetic resonance imaging: evaluating apparent diffusion coefficient values and biomarker expression in benign and malignant lesions. *Current Research in MRI*, 2023;2(3):50-54.

Corresponding author: Esra Bilici, e-mail: esra.bilici@hotmail.com

Received: June 23, 2023 **Accepted:** July 26, 2023 **Publication Date:** August 25, 2023

DOI:10.5152/CurrResMRI.2023.23059



Content of this journal is licensed under a Creative Commons Attribution-NonCommercial 4.0 International License.

ABSTRACT

Objective: In the literature, apparent diffusion coefficient values are known to be able to discriminate between benign and malignant breast lesions. We aim to evaluate the most efficient *b*-value to discriminate between benign and malignant lesions and also to reveal the potential relationships between diffusion-weighted imaging and apparent diffusion coefficient values and biomarker expression.

Methods: We retrospectively evaluated the magnetic resonance imaging and pathological data of 60 breast lesions, categorized as BI-RADS 4, 5, and 6. Signal intensity values obtained from diffusion-weighted imaging at B0, B1000 and apparent diffusion coefficient values were recorded. A possible correlation between apparent diffusion coefficient values and tumor grade, receptor expression (that of estrogen receptor, progesterone receptor, and human epidermal growth factor receptor 2), and Ki-67 score was investigated.

Results: Twenty-two (36.6%) lesions were malignant, and 38 (63.4%) lesions were benign. Mean apparent diffusion coefficient values of malignant lesions were significantly lower than that of benign lesions ($187 \pm 215 \times 10^{-6}$ and $625 \pm 118 \times 10^{-6}$ mm²/s, respectively). We detected lower apparent diffusion coefficient values in estrogen receptor- and progesterone receptor-negative tumors, also lower apparent diffusion coefficient values were correlated with higher Ki-67 index ($P < .05$). We cannot find any significant relationship between apparent diffusion coefficient values and human epidermal growth factor receptor 2 expression ($P > .05$). We showed that signal intensity values obtained at B1000 were more efficient than those obtained at B0 in differentiating benign and malignant lesions. Apparent diffusion coefficient values obtained from ipsilateral, pathologically proven metastatic lymph nodes were significantly lower from contralateral lymph nodes.

Conclusion: Apparent diffusion coefficient values can be used effectively to predict breast malignancy, estrogen receptor/progesterone receptor negativity, and Ki-67 index. Diffusion-weighted imaging obtained at B1000 is more effective in predicting malignancy compared to B0.

Keywords: ADC, biomarkers, breast cancer, DWI

INTRODUCTION

Breast cancer is a relatively common and potentially life-threatening disease that affects millions of women worldwide.¹ Early detection and accurate diagnosis are crucial in improving patient outcomes and reducing mortality rates. Over the years, imaging techniques have played a pivotal role in the diagnosis and management of breast cancer, enabling health-care professionals to detect lesions earlier, assess their characteristics, and guide treatment decisions.

Conventional imaging techniques, such as mammography (MG) and ultrasound (US), have long been the mainstay for breast cancer screening and evaluation. Mammography is widely used due to its ability to detect microcalcifications and architectural distortions associated with early-stage breast cancer. However, it has certain limitations, particularly in women with dense breast tissue, where the sensitivity of mammography may be reduced.² Ultrasound, on the other hand, is valuable for differentiating solid masses from cysts and guiding targeted biopsies. Despite their effectiveness, these techniques may not provide sufficient information for precise characterization of breast lesions, especially when it comes to distinguishing between benign and malignant cases³.

In recent years, diffusion-weighted imaging (DWI) has emerged as a promising modality for breast imaging. Diffusion-weighted imaging utilizes the random motion of water molecules within tissues to generate contrast and provide insights into tissue microstructure. It is based on the measurement of the apparent diffusion coefficient (ADC), which reflects the degree of water molecule diffusion within the tissue. By measuring

ADC values, DWI can offer valuable information about tissue cellularity, organization, and vascularity, which are essential in differentiating benign and malignant lesions.⁴

Diffusion-weighted imaging is a noninvasive technique, requires no ionizing radiation exposure, and does not require the administration of contrast medium. The short examination time, especially when using parallel imaging, is an additional advantage, as is the ability to assess the tumor completely. Furthermore, both conventional morphologic and physiologic assessments can be made during the same examination.⁵

Single-shot or multishot echo-planar imaging (EPI) is regarded as baseline techniques for DWI acquisition. On high *b*-values, cancers are typically hyperintense given adequate baseline T2 signal. As the basic DWI sequence is T2-weighted, lesions with higher water content will show a high signal on low *b*-value images and may retain a (relatively) high signal on high *b*-value images. Consequently, a high signal on high *b*-values images may be due to a very high T2 signal or true diffusion restriction with little signal decrease of a moderately high T2 signal.⁶

The ability of DWI to discriminate between benign and malignant breast lesions has been investigated extensively, and DWI has shown promising results. Malignant breast lesions generally exhibit lower ADC values due to their higher cellularity and restricted water diffusion.⁷ On the other hand, benign lesions, such as fibroadenomas or cysts, tend to have higher ADC values due to their lower cellularity and increased water diffusion.⁸

However, the role of DWI signal intensity (SI) values and the optimal selection of *b*-values in DWI for breast imaging remain as the areas of ongoing research. *B*-values represent the strength and timing of diffusion-sensitizing gradients used in DWI magnetic resonance imaging (DW-MRI). Different *b*-values can influence the sensitivity and specificity of DWI-MRI in detecting and characterizing breast lesions. Therefore, determining the most efficient *b*-value for discriminating

between benign and malignant lesions is essential for improving the accuracy and diagnostic performance of DWI.⁹

Furthermore, beyond the discrimination between benign and malignant lesions, DWI has the potential to provide valuable insights into the molecular characteristics of breast tumors.¹⁰ The correlation between ADC values and biomarker expression, such as that of estrogen receptor (ER), progesterone receptor (PR), human epidermal growth factor receptor 2 (HER-2), and the proliferation marker Ki-67, has been of great interest.¹¹ Understanding these relationships can aid in predicting tumor aggressiveness, assessing treatment response, and personalizing therapeutic strategies.

In this study, we aimed to evaluate the most efficient *b*-value in discriminating between benign and malignant breast lesions using DWI. Additionally, we aimed to investigate the potential relationships between DWI and ADC values and biomarker expression, including that of ER, PR, HER-2, and Ki-67. The findings from this research will contribute to the growing body of knowledge regarding the utility of DWI.

METHODS

Our study was a retrospective study and included patients who applied to our clinic between January 2022 and June 2022. Our study was approved by the Erzincan Binali Yıldırım University Ethics Committee (Ethics committee approval number: EBYU-KAEK-2023-4/21 E-1845473.11. ED.28465). A retrospective analysis was performed on MRI images and pathological data from 60 breast lesions classified as BI-RADS 4, 5, and 6. Patients reported as BI-RADS 4, 5, and 6 in the breast MRI report were included in the study. Inappropriate image quality was chosen as an exclusion criterion. Five patients were excluded from the study and 60 patients were included in the study.

Breast MRI examinations were performed with a 1.5-T whole-body imaging system (MAGNETOM Aera, Siemens, Erlangen, Germany). The patients were scanned in the prone position with the breast suspended in a 16-channel breast coil. Precontrast transverse acquisitions were performed using a T1-weighted fast spin echo sequence and transverse T2-weighted fast spin echo short-tau inversion recovery (STIR) imaging, while precontrast sagittal acquisitions were performed using a T2-weighted fast spin echo sequence imaging with fat suppression. Diffusion-weighted images were acquired with fat saturation using axial echo planar imaging (EPI) sequences at $b=1000$ s/mm² before contrast administration. Sagittal pre- and postcontrast dynamic imaging was performed using a 3D multiphase fast gradient echo pulse sequence. Additionally, transverse postcontrast T1-weighted images were acquired using the fast spoiled gradient-recalled echo sequence in the same manner as it was used to acquire the precontrast images, without a change in the patient's position. Subtraction images were created. The patients were given a bolus intravenous injection of gadolinium contrast (0.2 mmol/kg). Both morphological features and kinetic characteristics of the lesions were examined. Region of interest (ROI) values were made using circular ROI.

Then a possible correlation between ADC values and tumor grade, receptor expression (that of ER, PR, and HER-2), and Ki-67 score was investigated. ADC values from histologically diagnosed axillary lymph nodes were also analyzed.

All assessments were made by a single radiologist with 5 years of experience.

MAIN POINTS

- ADC values can be used effectively to predict breast malignancy, ER/PR receptor negativity and Ki-67 index. DWI obtained in B1000 is more effective in predicting malignancy compared to B0.
- DWI has been shown to have the ability to distinguish between benign and malignant breast lesions. Malignant breast lesions usually exhibit lower ADC values due to their higher cellularity and restricted water diffusion. On the other hand, benign lesions tend to have higher ADC values due to their lower cellularity and increased water diffusion.
- Of the 60 lesions, 22 (36.6%) were malignant and 38 (63.4%) were benign. The mean ADC values of malignant lesions were significantly lower than those of benign lesions ($187 \pm 215 \times 10^{-6}$ and $625 \pm 118 \times 10^{-6}$ mm²/s, respectively).
- Lower ADC values were observed in ER and PR negative tumors, and there was a positive correlation between lower ADC values and higher Ki-67 index.
- DWI with optimal *b*-values and ADC value analysis holds great promise as a valuable imaging technique in the evaluation of breast lesions. By providing non-invasive information about tumor characteristics, including malignancy, receptor expression, and proliferative activity, DWI can aid in clinical decision-making and contribute to improved patient management in breast cancer.

Statistical Analysis

Data were analyzed using the Statistical Package for the Social Sciences Statistics for Windows, version 20.0, software (IBM SPSS Corp., Armonk, NY, USA). Normal distribution of the data was evaluated with the Kolmogorov–Smirnov test. Numerical variables with normal distribution were shown as mean \pm standard deviation values. Student's *t*-test was used to analyze the difference between mean ADC values of the groups. Spearman's and Pearson's correlation analyses were applied to define possible correlations between the ADC values and pathological parameters. Logistic regression analysis was applied to define the diagnostic efficacy of the DWI SI values.

RESULTS

Of the 60 lesions, 22 (36.6%) were malignant and 38 (63.4%) were benign. The malignant group consisted of 6 cases (27.2%) of ductal carcinoma in situ, 10 cases (45.4%) of invasive ductal carcinoma, 5 cases (22.7%) of invasive lobular carcinoma, and 1 case (4.5%) of B-cell lymphoma. The benign group consisted of 22 cases (57.8%) of fibroadenoma, 7 cases (18.4%) of sclerosing adenosis, 5 cases (13.1%) of benign phyllode tumor, and 4 cases (10.5%) of usual ductal hyperplasia. The mean ADC values of malignant lesions were significantly lower than those of benign lesions ($187 \pm 215 \times 10^{-6}$ and $625 \pm 118 \times 10^{-6}$ mm²/s, respectively). The results are shown in Table 1.

There were 3 ER-negative and 7 PR-negative tumors, and ADC values of these receptor-negative tumors were lower ($187 \pm 215 \times 10^{-6}$ mm²/s). The level of the Ki-67 proliferation index was available for 23 patients. The mean value was $12.36 \pm 21.68\%$. A Ki-67 value of 25% was used as the threshold for discriminating between tumors with low Ki-67 expression (<25%) and high Ki-67 expression ($\geq 25\%$). And these tumors had a high Ki-67 expression ($\geq 25\%$). Ki-67 proliferation index was evaluated in 23 lesions; 12/23 had high and 11/23 had low index. Tumors with low expression of Ki-67 had higher ADC values than tumors with high expression of Ki-67 ($187 \pm 215 \times 10^{-6}$ and $625 \pm 118 \times 10^{-6}$ mm²/s, respectively; $P < .005$). It was observed that there was a positive correlation between them.

Lower ADC values were observed in ER- and PR-negative tumors, and there was a positive correlation between lower ADC values and higher Ki-67 index ($P < .05$). However, no significant relationship between ADC values and HER-2 expression was found. Diffusion-weighted imaging SI values obtained at $b=1000$ demonstrated higher efficiency in differentiating between benign and malignant lesions compared to $b=0$ ($P < .05$).

Furthermore, ADC values obtained from ipsilateral metastatic lymph nodes were significantly lower than (ADC values $187 \pm 215 \times 10^{-6}$) those from contralateral lymph nodes ($P < .05$).

Table 1. Lesion Characterization

	Total	Percent
Malignant group	32	36.6
Ductal carcinoma in situ	6	27.2
Invasive ductal carcinoma	10	45.4
Invasive lobular carcinoma	5	22.7
B-cell lymphoma	1	4.5
Benign group	38	64.4
Fibroadenoma	22	57.8
Sclerosing adenosis	7	18.4
Benign phyllode tumor	5	13.1
Usual ductal hyperplasia	4	10.5

Table 2. Estrogen Receptor (ER), Progesterone Receptor (PR), and c-erbB2 Amplification Characteristics of the Lesions

Pathological Diagnosis	ER		PR		c-erbB2	
	+	-	+	-	+	-
Ductal carcinoma in situ	6	0	5	1	4	2
Invasive ductal carcinoma	8	2	6	4	5	5
Invasive lobular carcinoma	4	1	3	2	2	3
B-cell lymphoma	1	0	1	0	0	1
Total	19	3	15	7	11	1

Twenty-one of 60 (35.5%) patients had histopathologically proven metastatic axillary lymph nodes on MR images; 39/60 (65%) patients did not have any pathological axillary lymph node.

Estrogen receptor (ER), progesterone receptor (PR), and c-erbB2 amplification characteristics of lesions are shown in Table 2.

Case examples can be seen in Figures 1-3.

DISCUSSION

Our findings demonstrated that ADC values obtained from DWI can serve as an effective tool in predicting breast malignancy, as evidenced by the significantly lower mean ADC values observed in malignant lesions compared to benign lesions. These results are consistent with previous studies like Razek et al's study that have reported lower ADC values in malignant breast tumors due to their higher cellularity and restricted water diffusion.⁵ Therefore, ADC values derived from DWI can provide valuable information for differentiating between benign and malignant breast lesions.

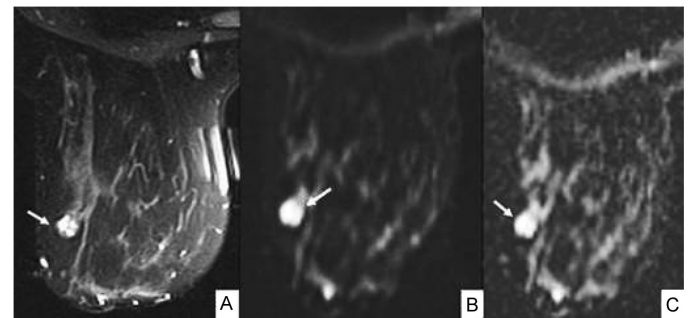


Figure 1. Contrast enhanced axial image (a), DWI (b), and ADC map (c) of a benign lesion (fibroadenoma).

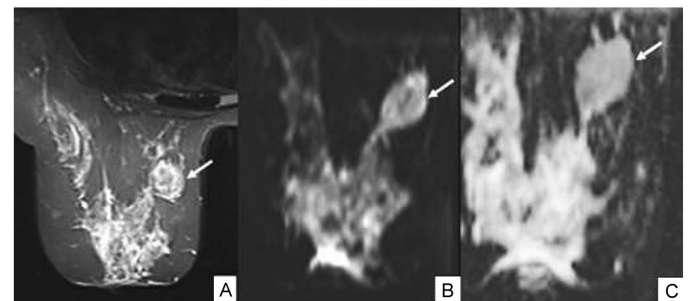


Figure 2. Contrast-enhanced axial image (A), DWI (B), and ADC map (C) of a malignant lesion (DIS). Apparent diffusion coefficient value of the lesion at B1000 is 143×10^{-6} . ADC, apparent diffusion coefficient; DIS, I added wrong figures, I need to delete and the rights, dissemination in space; DWI, diffusion-weighted imaging.

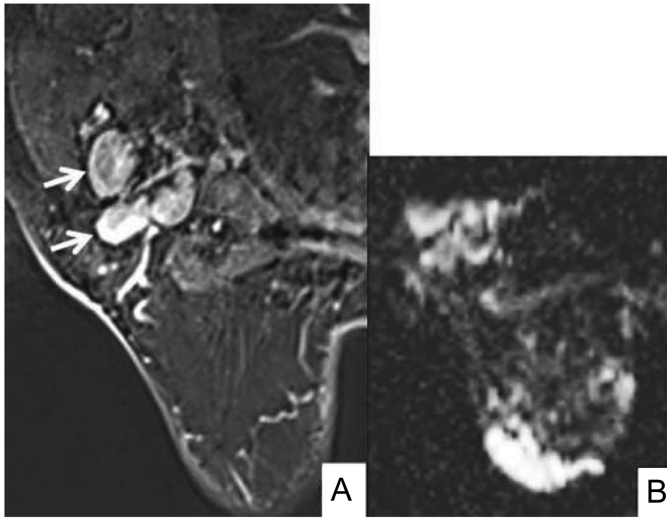


Figure 3. Contrast-enhanced axial image (A), and ADC map (B) of a histologically proven malignant axillary lymph node (invasive ductal carcinoma metastasis). Apparent diffusion coefficient value at B1000 is 810×10^{-6} . ADC, apparent diffusion coefficient.

Furthermore, Kim et al's study shows similar results to our study; our study revealed important associations between ADC values and biomarker expression. Lower ADC values were observed in ER- and PR-negative tumors, suggesting a potential link between decreased water diffusion and nonexistence of hormone receptor.¹²

Additionally, Surov et al's study shows similar results to our study; we found that lower ADC values correlated with a higher Ki-67 index, indicating a potential relationship between limited water diffusion and increased tumor proliferation. These findings highlight the potential of DWI and of ADC values as noninvasive biomarkers for predicting tumor grade and assessing the aggressiveness of breast cancer.¹³

Regarding the selection of b -values, our study demonstrated that SI values obtained at b1000 were more efficient than those obtained at B0 in differentiating benign and malignant lesions. This suggests that higher b -values may provide more accurate information to detect and characterize breast lesions, similar to the results of the Kuroki et al's study.¹⁴

Our study revealed that ADC values in axillary lymph nodes ipsilateral, pathologically proven metastatic lymph nodes were significantly lower than in contralateral normal lymph nodes, as in the study of Fornasa et al.¹⁵

Guo et al's study shows similar results to our study that the ADC is useful in differentiating benign from malignant breast lesions.¹⁶

Breast cancer is now a significant cause of worldwide morbidity and mortality. Further, the increasing rate of breast cancer continues to be a major area of concern for both clinicians and researchers. Increased awareness in the affected population leads to more frequent physical examinations and diagnostic imaging procedures; thus, it can be expected to result in an earlier diagnosis and hence improved prognosis.¹³

The results of this study indicate that ADC values can effectively predict breast malignancy, ER and PR negativity, and Ki-67 index.

Diffusion-weighted images obtained at $b=1000$ provides higher efficiency in predicting malignancy compared to $b=0$. Axillary metastatic lymph nodes exhibit lower ADC values compared to contralateral normal lymph nodes. Lower ADC values were observed in ER- and PR-negative tumors, suggesting a potential link between decreased water diffusion and nonexistence of hormone receptor. Additionally, lower ADC values were correlated with a higher Ki-67 index, indicating a potential association between restricted water diffusion and increased tumor proliferation. Optimizing the selection of b -values in DWI protocols can improve the diagnostic performance and reliability of this imaging modality for breast cancer evaluation.

These findings and the findings in the literature highlight the potential of DWI and ADC values in improving the characterization and assessment of breast lesions, aiding in treatment planning and patient management.

Study Limitations

The main limitations of our study were the retrospective design and the relatively small sample size. Further large-scale prospective studies are warranted to validate our findings and explore additional correlations between DWI-MRI, biomarker expression, and clinical outcomes. Also, the fact that MR measurements were made by the same radiologist is a limitation.

Ethics Committee Approval: Ethics committee approval was received for this study from the ethics committee of Erzincan Binali Yıldırım University (Date: April 21, 2023 No.: E-1845473.11. ED:28465).

Informed Consent: Due to the retrospective design of the study, informed consent was not obtained.

Peer-review: Externally peer-reviewed.

Author Contributions: Concept – D.C., E.B., T.Ç.; Design – D.C.; Supervision – T.K.; Materials – E.B.; Data Collection and/or Processing – E.B.; Analysis and/or Interpretation – T.Ç.; Literature Search – T.K., T.Ç.; Writing Manuscript – D.C., T.K.; Critical Review – E.B., T.Ç.

Declaration of Interests: The authors declare that they have no competing interest.

Funding: The authors declared that this study has received no financial support.

REFERENCES

1. World Health Organization. *Breast Cancer: Prevention and Control*. Available at: <https://www.who.int/cancer/detection/breastcancer/en/>.
2. Kolb TM, Lichy J, Newhouse JH. Comparison of the performance of screening mammography, physical examination, and breast US and evaluation of factors that influence them: an analysis of 27,825 patient evaluations. *Radiology*. 2002;225(1):165-175. [CrossRef]
3. Balleyguier C, Opolon P, Mathieu MC, et al. Nonpalpable breast carcinoma: review of 1000 cases with radiologic-pathologic correlations. *Radiology*. 1995;197(3):825-832.
4. Woodhams R, Matsunaga K, Iwabuchi K, et al. Diffusion-weighted imaging of malignant breast tumors: the usefulness of apparent diffusion coefficient (ADC) value and ADC map for the detection of malignant breast tumors and evaluation of cancer extension. *J Comput Assist Tomogr*. 2005;29(5):644-649. [CrossRef]
5. Abdel Razek AAKA, Gaballa G, Denewer A, Tawakol I. Diffusion weighted MR imaging of the breast. *Acad Radiol*. 2010;17(3):382-386. [CrossRef]
6. Baltzer P, Mann RM, Iima M, et al. Diffusion-weighted imaging of the breast—a consensus and mission statement from the EUSOBI International Breast Diffusion-Weighted Imaging working group. *Eur Radiol*. 2020;30(3):1436-1450. [CrossRef]

7. Luo N, Su D, Jin G, Liu H. Diffusion-weighted MRI in the characterization of breast lesions: the optimal b-value for differentiating benign and malignant breast lesions. *Eur Radiol.* 2019;29(3):1388-1395.
8. D'Orsi CJ, Sickles EA, Mendelson EB, Morris EA. *ACR BI-RADS® Atlas, Breast Imaging Reporting and Data System.* American College of Radiology; 2013: 5.
9. Partridge SC, DeMartini WB, Kurland BF, Eby PR, White SW, Lehman CD. Quantitative diffusion-weighted imaging as an adjunct to conventional breast MRI for improved positive predictive value. *AJR Am J Roentgenol.* 2009;193(6):1716-1722. [\[CrossRef\]](#)
10. Thomassin-Naggara I, De Bazelaire C, Chopier J, Bazot M, Marsault C, Trop I. Diffusion-weighted MR imaging of the breast: advantages and pitfalls. *Eur J Radiol.* 2013;82(3):435-443. [\[CrossRef\]](#)
11. Bogner W, Pinker K, Zaric O, et al. Bilateral diffusion-weighted MR imaging of breast tumors with submillimeter resolution using readout-segmented echo-planar imaging at 7 Tesla. *Invest Radiol.* 2014;49(6): 380-386.
12. Kim JY, Kim JJ, Hwangbo L, et al. Diffusion-weighted MRI of estrogen receptor-positive, HER2-negative, node-negative breast cancer: association between intratumoral heterogeneity and recurrence risk. *Eur Radiol.* 2020;30(1):66-76. [\[CrossRef\]](#)
13. Surov A, Clauser P, Chang YW, et al. Can diffusion-weighted imaging predict tumor grade and expression of Ki-67 in breast cancer? A multicenter analysis. *Breast Cancer Res.* 2018;20(1):58. [\[CrossRef\]](#)
14. Kuroki Y, Nasu K. Advances in breast MRI: diffusion-weighted imaging of the breast. *Breast Cancer.* 2008;15(3):212-217. [\[CrossRef\]](#)
15. Fornasa F, Nesoti MV, Bovo C, Bonavina MG. Diffusion-weighted magnetic resonance imaging in the characterization of axillary lymph nodes in patients with breast cancer. *J Magn Reson Imaging.* 2012;36(4):858-864. [\[CrossRef\]](#)
16. Guo Y, Cai YQ, Cai ZL, et al. Differentiation of clinically benign and malignant breast lesions using diffusion-weighted imaging. *J Magn Reson Imaging.* 2002;16(2):172-178. [\[CrossRef\]](#)

Magnetic Resonance Imaging Examination for the Detection of Cranial Complications in Pediatric Patients with Post-Coronavirus Disease 2019 Infection

Ömer Kazcı 

Department of Radiology, Presidential Health Services Center, Ankara, Turkey

Cite this article as: Kazcı Ö. Magnetic resonance imaging examination for the detection of cranial complications in pediatric patients with post-coronavirus disease 2019 infection. *Current Research in MRI*, 2023;2(3):55-58.

Corresponding author: Omer Kazci, e-mail: omerkazci1990@gmail.com

Received: June 25, 2023 **Accepted:** July 17, 2023 **Publication Date:** August 19, 2023

DOI:10.5152/CurrResMRI.2023.23060



Content of this journal is licensed under a Creative Commons Attribution-NonCommercial 4.0 International License.

Abstract

Objective: Coronavirus disease 2019, caused by the novel coronavirus severe acute respiratory syndrome coronavirus 2, has affected millions of people worldwide since its emergence in late 2019. Although children generally experience milder symptoms compared to adults, there have been reports of severe cases and post-infectious complications, including neurological manifestations. This article discusses the role of magnetic resonance imaging in detecting cranial complications in pediatric patients with a history of coronavirus disease 2019 infection.

Methods: In our study, we retrospectively scanned the images of 246 pediatric patients who had coronavirus disease 2019 between April 2020 and June 2022 and then underwent cranial magnetic resonance imaging with diverse complaints at a tertiary healthcare center. Pathologies that were identified were classified and recorded as final data.

Results: In a study of 246 pediatric coronavirus disease 2019 patients, neurological complications were relatively rare. Most children experience mild or asymptomatic cases. Serious complications such as multisystem inflammatory syndrome in children developed in 8 patients (3%), acute disseminated encephalomyelitis developed in 10 patients (4%), a cerebral vascular infarct developed in 20 patients (8%), non-specific T2 Weight imaging and Fluid attenuated Inversion Recovery(T2WI -Flair) hyperintensity developed in 120 patients (48.6%), and meningoencephalitis developed in 10 patients (4%).

Conclusion: Of the patients examined in our study, 67.8% exhibited pathology. T2WI and FLAIR sequences revealed non-specific hyperintensity foci as the most prevalent pathology. Further research is needed to determine the optimal timing and indications for magnetic resonance imaging in this population, as well as the correlation between magnetic resonance imaging findings and long-term neurological outcomes.

Keywords: Complications, magnetic resonance imaging, post-COVID-19, stroke, T2WI hyperintensity

INTRODUCTION

The coronavirus disease 2019 (COVID-19) pandemic, caused by the severe acute respiratory syndrome coronavirus 2 (SARS-CoV-2), has had a significant global impact on public health and healthcare systems since its emergence in late 2019. While the majority of COVID-19 cases have been reported in adults, children, and adolescents are not immune to the infection, and they can also experience both acute and long-term complications.^{1,2} Although pediatric patients with COVID-19 generally exhibit milder symptoms compared to adults, emerging evidence suggests that some children may develop post-acute sequelae of SARS-CoV-2 infection or “long COVID,” with symptoms persisting for months after the acute phase of the infection.¹ Among these complications, neurological manifestations have been increasingly recognized, including meningoencephalitis, acute disseminated encephalomyelitis (ADEM), Guillain-Barré syndrome (GBS), and acute flaccid myelitis.³

Magnetic resonance imaging (MRI) is a non-invasive, radiation-free imaging modality that has been widely employed to detect and characterize various neurological complications in both adult and pediatric patients with COVID-19.⁴ In particular, MRI has proven to be a valuable tool for detecting inflammatory and ischemic changes, white matter abnormalities, and other cerebral lesions in patients with neurological manifestations of COVID-19.⁵

In this article, we aim to provide an overview of the role of MRI in detecting and characterizing cranial complications in pediatric patients with a post-COVID-19 infection. We will discuss the various MRI findings associated with different neurological complications as well as the potential mechanisms underlying these abnormalities. Furthermore, we will explore the clinical implications of these findings and the challenges of differentiating between primary COVID-19-related neurological complications and those resulting from other etiologies.

METHODS

In our study, we retrospectively scanned the images of 246 pediatric patients who had COVID-19 between April 2020 and June 2022 and then underwent cranial MRI with diverse complaints at a tertiary health-care center. Since our study was retrospective, we did not obtain ethical approval. After recovering from COVID-19, we included patients between the ages of 1 and 17 who presented with diverse complaints. Our study excluded patients with congenital diseases, tumors, epilepsy, hydrocephalus, etc. Pathologies that were identified were classified and recorded as final data.

Magnetic Resonance Imaging Protocol

A cranial MRI scan taken with a 1.5-T (Magnetom Aera, Siemens Healthineers, Erlangen, Germany) MR machine is a non-invasive imaging test that uses a powerful magnetic field and radio waves to produce detailed images of the brain and surrounding structures. The technical parameters for a typical cranial MRI may include a magnetic field strength of 1.5 Tesla and various sequence types such as T1-weighted, T2-weighted, Fluid attenuation inversion recovery (FLAIR), Diffusion Weighted Imaging (DWI), and Gradient echo sequences (GRE). The slice thickness is typically 3 mm or less, and the matrix size is usually 256×256 or higher. The field of view is typically 22-24 cm, and the scan time can range from 15 to 30 minutes for a routine cranial MRI. The repetition time (TR) and echo time (TE) may vary depending on the sequence type and specific imaging parameters but typically range from 2000 to 6000 ms for TR and 80-150 ms for TE. The flip angle may vary from 90° to 180° .

Statistical Analysis

Descriptive analyses were performed to summarize the data collected in the study. For categorical variables, frequency tables were used to present the distribution of the different categories, while for continuous variables, such as age, the mean and standard deviation (\pm SD) were calculated, along with the minimum (min) and maximum (max) values observed.

RESULTS

In a study of 246 pediatric COVID-19 patients, 100 of the scanned images were of females and 146 were of males. The patients were between 1 and 17 years old. The mean age was 9.87 ± 4.69 (min: 1; max: 17). The mean age of girls is 10.5 (min: 1-max: 17). The mean age of boys is 9.5 (min: 1-max: 17). Serious complications such as multisystem inflammatory syndrome in children (MIS-C) (Figure 1) developed in 8 patients (3%), ADEM developed in 10 patients (Figure 2) (4%), cerebrovascular infarct (Figure 3) developed in 20 patients (8%), non-specific T2 Weight and Fluid Attenuation Inversion Recovery (T2WI-FLAIR) hyperintensity (Figure 4) developed in 120 patients (48%, 6%), and meningoencephalitis (Figure 5) developed in 10 patients (4%). The defined data are shown in Table 1.

MAIN POINTS

- Classification of cranial complications after Covid 19 infection in pediatric patients by MRI
- Detection of the most common neurological finding after covid in pediatric patients
- Classification of neurological complications after covid in pediatric patients by age and gender

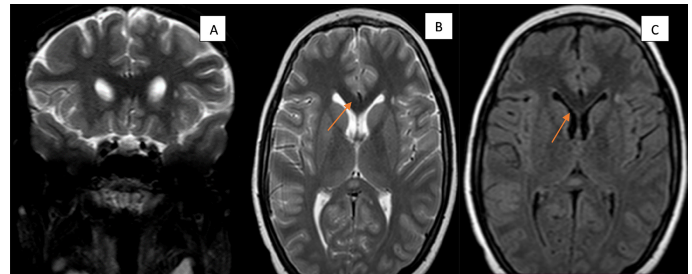


Figure 1. Left periventricular hyperintense lesion in an 8-year-old child with MIS-C after COVID was observed on frontal subcortical (indicated by an arrow). (A) Coronal T2WI, (B) axial T2WI, and (C) FLAIR sequences. MIS-C, multisystem inflammatory syndrome in children; COVID, coronavirus disease.

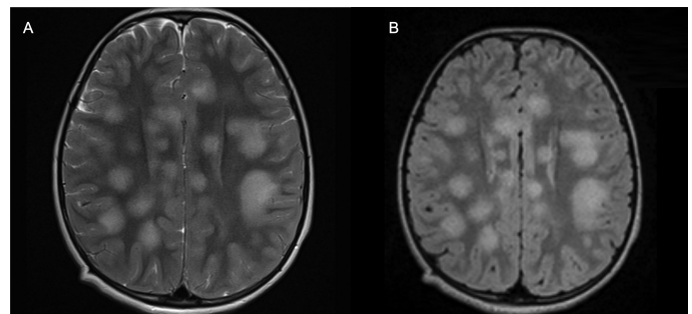


Figure 2. A 11-year-old girl was diagnosed with acute disseminated encephalomyelitis (ADEM). She had hyperintense plaque formations in the periventricular white matter and the centrum semiovale. (A) T2 Weight Imaging T2WI and (B) Fluid attenuation recovery FLAIR scans.

DISCUSSION

The COVID-19 pandemic has had significant and wide-ranging effects on global health, with numerous complications and sequelae identified in both adult and pediatric populations. Children, while generally experiencing milder symptoms during the acute phase of the infection, are not immune to the post-acute sequelae of the SARS-CoV-2 infection.^{1,2} As a result, it is crucial to investigate the potential complications and long-term effects of COVID-19 in pediatric patients. One area of particular concern is the potential for cranial complications, which can have significant impacts on cognitive, emotional, and physical development. Magnetic resonance imaging examinations have been

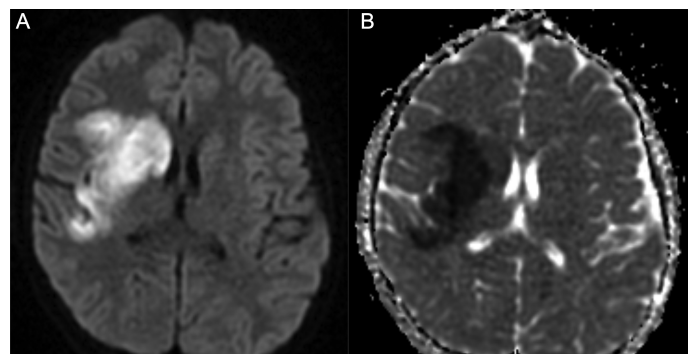


Figure 3. Fourteen days after COVID, a 15-year-old male patient developed an infarct in the right Middle Cerebral Artery (MCA) irrigation area. (A) Diffusion weighted imaging (DWI) and (B) apparent diffusion coefficient (ADC). COVID, coronavirus disease.

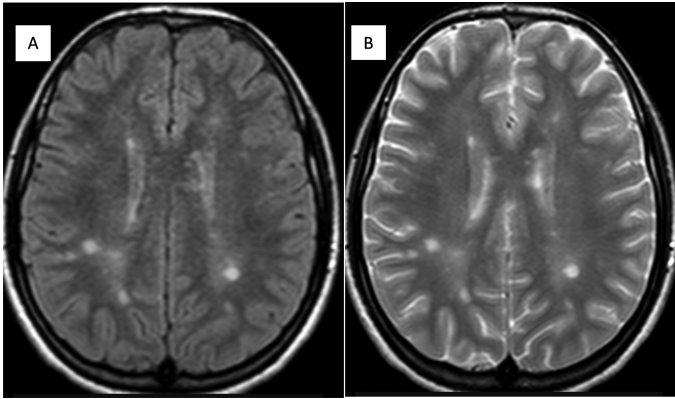


Figure 4. On the MRI of a 17-year-old female patient with headache after COVID, a few non-specific (A) T2 Weight and Fluid Attenuation Inversion Recovery (T2WI) (B) FLAIR hyperintense foci located posteriorly in the periventricular white matter and centrum semiovale observed 2 months after COVID. COVID, coronavirus disease; MRI, magnetic resonance imaging.

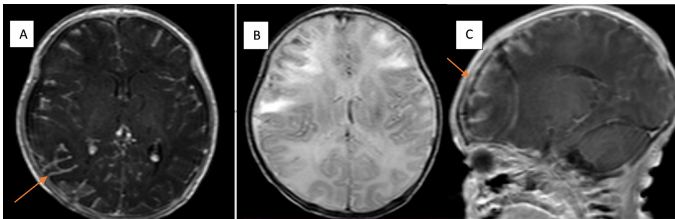


Figure 5. A 4-year-old boy patient with meningoencephalitis after COVID (indicated by an arrow) (A) On the post-contrast T1 Weight Imaging (T1WI) axial image cranial MRI, dural thickening and meningeal enhancement were observed at the right back parietal level. (B) On the axial Fluid Attenuation Inversion Recovery (FLAIR) image, cortical-subcortical edema is observed. (C) Increased enhancement of the meninges and dura is observed on sagittal T1WI sagittal image. COVID, coronavirus disease; MRI, magnetic resonance imaging.

proposed as a valuable tool for detecting these complications in pediatric patients. Severe acute respiratory syndrome coronavirus 2 can potentially invade the nervous system, including the brain, either via the bloodstream or by crossing the nasal cavity and entering the olfactory nerve, which connects directly to the brain. The virus has been found in brain tissue and cerebrospinal fluid in some cases, but not consistently. The body's immune response to the virus can lead to a state of systemic inflammation. When this inflammation involves the brain and nervous system, it can potentially result in various neurological complications. This mechanism is supported by the observation that many people with severe COVID-19 have high levels of inflammatory markers in their blood, even if the virus cannot be detected in their nervous system. Coronavirus disease 2019 can lead to a state of increased blood

clotting, which can result in strokes even in young, healthy individuals. This increased clotting can potentially lead to other neurological complications as well if it affects blood flow to the brain. After the acute phase of COVID-19, some individuals may experience a post-infectious autoimmune reaction, where the immune system mistakenly attacks the body's own tissues instead of the virus. This is thought to be the mechanism behind some cases of GBS following COVID-19. Emerging research suggests that the virus might trigger neurodegenerative processes in the brain leading to symptoms similar to Parkinson's disease or Alzheimer's disease. However, much more research is needed to confirm and understand these potential effects. It is important to note that these mechanisms are not mutually exclusive and could all contribute to the neurological complications observed in different individuals. In fact, individual variations in factors like genetics, immune response, and viral load could potentially explain why different people experience different neurological complications following COVID-19.

Magnetic resonance imaging has been widely recognized as a non-invasive and highly effective imaging modality for detecting and diagnosing various neurological disorders.⁶ A growing body of evidence suggests that COVID-19 can lead to neurological complications in both adults and children, including encephalopathy, seizures, and cerebrovascular accidents.^{7,8} As such, the use of MRI to assess the risk of cranial complications in pediatric patients with a post-COVID-19 infection is a logical and well-supported approach.

Recent studies have reported various neurological complications in pediatric patients with COVID-19, such as ADEM, acute necrotizing encephalopathy, and GBS.⁹ In addition, the MIS-C associated with COVID-19 can also present with neurological symptoms. These conditions may cause significant morbidity and long-term sequelae, making early detection and intervention crucial. Magnetic resonance imaging has also been instrumental in the diagnosis of MIS-C, a condition that can present with encephalopathy, seizures, and focal neurological deficits.¹⁰ A case report by LaRovere et al described the use of MRI in diagnosing a pediatric patient with MIS-C and encephalopathy, highlighting the importance of MRI in the early detection of cranial complications in such patients.¹² In another case report published by Karavas et al, they described a rare case of COVID-19-associated acute necrotic encephalopathy in a 2-year-old child.¹⁴

In another study by Lindan et al,⁸ MRI findings in 50 pediatric patients with post-acute sequelae of SARS-CoV-2 infection were assessed. The study reported that 60% of the patients exhibited abnormal findings, including white matter hyperintensities, leptomeningeal enhancement, and punctate ischemic lesions. These findings underscore the importance of MRI in detecting subtle cranial complications in pediatric patients with post-infection. Another study by Abdel-Mannan et al¹³ evaluated 27 pediatric patients with neurological complications associated with COVID-19. Of these, 67% showed abnormalities on brain MRI, including leptomeningeal enhancement, myelitis, and encephalitis. Furthermore, the study found a correlation between the severity of neurological manifestations and extraabnormalities.

In another study by Gaur et al, the authors identified several MRI features that were associated with neurological complications in children with COVID-19, including intracranial hemorrhage, white matter abnormalities, and brainstem lesions.⁶

In our study, we examined patients who had recovered from 246 COVID-19 cases and subsequently underwent cranial MRI for various

Table 1. Distribution of Neurocranial Pathologies

	n	%
ADEM (acute disseminated encephalomyelitis)	10	4
Encephalitis	10	4
Infarct	20	8
MIS-C (multisystem inflammatory syndrome in children)	8	3,2
Non-specific T2WI-FLAIR hyperintensity	120	48,6
Normal	78	32,2
Total	246	100,0

complaints. Pathology was identified in 67.8% of patients. Compared to the studies mentioned in the preceding paragraph, the patient population in our study was larger, and the diversity and pathology detection rates were greater and more inclusive. The age spectrum of patients was kept broad.

Our research has a number of limitations. As with any descriptive study, increasing the population size yields more accurate results. Only the pediatric population was evaluated; adult patients were not studied. One of the study's limitations is that it did not evaluate patients aged 0-1 years, and the number of patients aged 1-7 years is relatively low compared to other age groups.

Of the patients examined in our study, 67% exhibited pathology. The T2WI and FLAIR sequences revealed non-specific hyperintense foci as the most prevalent pathology. Further research is needed to determine the optimal timing and indications for MRI in this population, as well as the correlation between MRI findings and long-term neurological outcomes.

Ethics Committee Approval: Ethical approval was not required as it was a retrospective study and the data were collected from the data pool.

Informed Consent: Since the data were collected from the data pool, patient consent was not obtained.

Peer-review: Externally peer-reviewed.

Declaration of Interests: The author declare that they have no competing interest.

Funding: The author declared that this study has received no financial support.

REFERENCES

1. Ludvigsson JF. A systematic review of COVID-19 in children shows milder cases and a better prognosis than adults. *Acta Paediatr.* 2020;109(6):1088-1095. [\[CrossRef\]](#)
2. Aydin S, Unver E, Karavas E, Yalcin S, Kantarci M. Computed tomography at every step: long-term coronavirus disease. *Respir Investig.* 2021;59(5):622-627. [\[CrossRef\]](#)
3. Liguoro I, Pilotto C, Bonanni M, et al. SARS-CoV-2 infection in children and newborns: a systematic review. *Eur J Pediatr.* 2020;179(7):1029-1046. [\[CrossRef\]](#)
4. Cohen ME, Eichel R, Steiner-Birmanns B, et al. A case of probable Parkinson's disease after SARS-CoV-2 infection. *Lancet Neurol.* 2020;19(10):804-805. [\[CrossRef\]](#)
5. Katal S, Johnston SK, Johnston JH, Gholamrezanezhad A. Imaging findings of SARS-CoV-2 infection in pediatrics: a systematic review of coronavirus disease 2019 (COVID-19) in 850 patients. *Acad Radiol.* 2020;27(12):1608-1621. [\[CrossRef\]](#)
6. Gaur P, Dixon L, Jones B, Lyall H, Jan W, Kneen R. Cranial imaging in children with COVID-19 infection presenting with neurological symptoms. *Dev Med Child Neurol.* 2021;63(5):573-579.
7. Huisman TAGM. Pediatric neuroimaging: from basic to advanced magnetic resonance imaging (MRI) techniques. *Neuroimaging Clin N Am.* 2016;26(2):343-354.
8. Lindan CE, Mankad K, Ram D, et al. Neuroimaging manifestations in children with SARS-CoV-2 infection: a multinational, multicenter collaborative study. *Lancet.* 2021;5(3):167-177.
9. Mao L, Jin H, Wang M, et al. Neurologic manifestations of hospitalized patients with coronavirus disease 2019 in Wuhan, China. *JAMA Neurol.* 2020;77(6):683-690. [\[CrossRef\]](#)
10. Mirzaee SMM, Gonçalves FG, Mohammadifard M, Tavakoli SM, Vosough A. Focal cerebral arteriopathy in a pediatric patient with COVID-19. *Radiology.* 2021;298(2):E98-E99.
11. Feldstein LR, Rose EB, Horwitz SM, et al. Multisystem inflammatory syndrome in U.S. children and adolescents. *N Engl J Med.* 2020;383(4):334-346. [\[CrossRef\]](#)
12. LaRovere KL, Riggs BJ, Poussaint TY, et al. Neurologic involvement in children and adolescents hospitalized in the United States for COVID-19, or multisystem inflammatory syndrome. *JAMA Neurol.* 2021;78(5):536-547. [\[CrossRef\]](#)
13. Abdel-Mannan O, Eyre M, Löbel U, et al. Neurologic and radiographic findings associated with COVID-19 infection in children. *JAMA Neurol.* 2021;77(11):1440-1445.
14. Karavas E, Tokur O, Topal I, Aydin S. Acute necrotizing encephalopathy associated with COVID-19 infection in a child J Clin Images. *Med Case Rep.* 2022;3(2):1657.

Ratio of Incidentally Detected Brain Tumors in Diffusion Magnetic Resonance Imaging Scans Performed in the Emergency Department on the Suspicion of Acute Stroke

Eren Tobcu¹, Erdal Karavaş¹, Özlem Çelik Aydın², Bilgin Topçu³

¹Department of Radiology, Bandırma Onyedi Eylül University School of Medicine, Bandırma Research and Training Hospital, Balıkesir, Turkey

²Department of Pharmacology, Erzincan Binali Yıldırım University, Faculty of Medicine Erzincan, Turkey

³Department of Radiology, Bandırma Research and Training Hospital, Balıkesir, Turkey

Cite this article as: Tobcu E, Karavaş E, Çelik Aydın Ö, Topçu B. Ratio of incidentally detected brain tumors in diffusion magnetic resonance imaging scans performed in the emergency department on the suspicion of acute stroke. *Current Research in MRI*, 2023;2(3):59-62.

Corresponding author: Eren Tobcu, e-mail: drerentobcu@gmail.com

Received: August 04, 2023 **Accepted:** September 29, 2023 **Publication Date:** October 23, 2023

DOI:10.5152/CurrResMRI.2023.23077



Content of this journal is licensed under a Creative Commons Attribution-NonCommercial 4.0 International License.

Abstract

Objective: The aim of the study was to analyze the incidence of newly diagnosed brain tumors in diffusion magnetic resonance imaging (MRI) scans conducted in the emergency department of a tertiary care hospital.

Methods: In this retrospective study, we analyzed diffusion MRI examinations retrospectively with the preliminary diagnosis of acute stroke in the emergency department of a tertiary care hospital in Balıkesir in June 2023 and July 2023. We identified patients with brain tumors on diffusion MRI images and performed basic statistical analysis.

Results: Among 1544 patients, 121 patients were diagnosed with acute intracranial infarction (54 females and 67 males, median age: 71), and intracranial tumors were identified in 10 patients (5 females and 5 males, median age: 59.4). Further imaging methods were used to characterize the tumors. Intracranial tumors of 3 patients were diagnosed as metastasis, and the masses of 2 patients were pathologically diagnosed as glioblastoma multiforme. The masses of 3 patients were diagnosed with meningioma after radiological examinations. A cystic mass was observed at the level of the fourth ventricle in 1 patient, and a porencephalic cyst was diagnosed in the left frontal cortex in 1 patient.

Conclusion: Diffusion-weighted imaging (DWI) is the first-line radiological imaging method with computed tomography for the evaluation of stroke patients in emergency departments. Therefore, we think that it is crucial to report other radiological findings besides acute stroke on DWI images and to guide the physician about advanced radiological methods for characterization of lesions.

Keywords: Diffusion MRI, acute stroke, brain tumor

INTRODUCTION

Although there has been a decrease in the occurrence of ischemic strokes in recent decades, it continues to be the primary cause of mortality and morbidity in Western countries.¹ Magnetic resonance imaging (MRI) is considered the most effective modality for the detection of early signs of cerebral ischemia.² Diffusion-weighted imaging (DWI) is a widely utilized MRI technique that is commonly performed for the evaluation of patients affected by stroke.³ The DWI technique has the capability to detect ischemic areas shortly after their initiation.⁴ Acute arterial ischemic stroke (AIS) can be observed on DWI as a hyperintense signal after a few minutes. This is accompanied by a decrease in the apparent diffusion coefficient (ADC).⁵

The term “brain tumor” encompasses a wide range of cancers that originate from various cells within the brain (known as primary tumors) or from tumors that have spread to the brain from other parts of the body (known as metastatic tumors). Primary brain tumors encompass a variety of histologic types that exhibit diverse gross and molecular characteristics. These tumors are categorized according to the World Health Organization classification of tumors of the central nervous system (CNS).⁶ Brain and other CNS tumors rank as the eighth most prevalent form of cancer among adults aged 40 and above.⁷ The incidence of nonmalignant brain and other CNS tumors in adults aged 20 and above is 22.38 per 100 000, indicating that the majority of diagnosed tumors in this age group are nonmalignant, while the incidence of malignant brain and other CNS tumors is relatively low in this particular age group, with an age-adjusted incidence rate of 8.5 per 100 000.^{7,8} In this retrospective study we analyzed the incidence of newly diagnosed brain tumors in diffusion MRI scans conducted in the emergency department of a tertiary care hospital in Turkey.

METHODS

In this retrospective study, we analyzed diffusion MRI examinations (GE 1.5T, 60 cm, SIGNA™ Creator/Explorer, China, 2017) with the preliminary diagnosis of acute stroke in the emergency department of a tertiary care hospital in Balikesir in June 2023 and July 2023. Patients between the ages of 19 and 99 who presented to the emergency department were included in the study. We only utilized 2 b values (0 and 1000 s/mm²) for DWI in this system. The typical imaging parameters were echo time=118, 128 × 128 matrix, 260 × 260 field of view, and 7 mm section thickness. We identified patients with brain tumors on diffusion MRI images and performed basis statistical analysis. The medical histories of identified patients were scanned using the hospital data processing system and the national medical patient registry system. Patients with known primary malignancy or intracranial tumors were excluded from the study. This research has been approved by the ethical committee of Erzincan Binali Yildirim University-kaek-2023-09-01-14572389.E1359002 (date: September 7, 2023), and the study was conducted in accordance with the Declaration of Helsinki.

RESULTS

The MRI images of a total of 1553 patients who underwent diffusion MRI for suspected acute stroke in the emergency department in June and July were analyzed retrospectively. A total of 9 patients with a primary malignancy or known intracranial mass were excluded from the study. Of 1544 patients, 841 were female and 703 were male; the mean age was 59.9. The demographic data of the patients are shown in Table 1. Among 1544 patients, 121 patients were diagnosed with acute intracranial infarction (54 females and 67 males, median age: 71), and intracranial tumors were identified in 10 patients (5 females and 5 males, median age: 59.4), and further imaging techniques were used to characterize the tumors.

On the basis of contrast-enhanced MRI examinations for tumor characterization on 3 patients diagnosed with tumors on diffusion MRI images, it was considered that the masses were predominantly compatible with metastasis (Figure 1). In the radiological imaging methods performed for primary tumor localization research, 2 of these patients were diagnosed with lung cancer and 1 with colon cancer. These diagnoses were then confirmed pathologically. On CT and MR images acquired after diffusion MRI, the masses of 2 patients primarily exhibited primary glial tumor characteristics (Figure 2). The patients underwent surgery, and their pathology results were reported as GBM.

Three patients with extra-axial mass on diffusion MR images were diagnosed with meningioma (Figure 3) with CT and MRI examinations performed after diffusion MR, and elective operation was

Table 1. Patient Demographics

Demographics	n	Mean Age
Number of diffusion-weighted images analyzed	1553	59.9
Female	846	59.7
Male	706	60.1
Number of patients with acute intracranial infarct	121	71
Female	54	71.8
Male	67	70.4
Number of patients with intracranial mass	10	59.4
Female	5	65.2
Male	5	53.6

planned by neurosurgery team. One patient had a simple cystic mass at the level of the fourth ventricle. The patient was sent to another center for surgery, but the patient's medical records could not be accessed afterward. One patient had a cystic mass reaching 5 cm in diameter in the left frontotemporal region, and a porencephalic cyst was diagnosed in conventional MRI imaging performed after diffusion MRI (Figure 4).

DISCUSSION

The initial clinical application of DWI was in brain tumors. Le Bihan et al⁹ published an article in 1986 describing intravoxel incoherent motion imaging, which incorporated diffusion imaging using a spin echo sequence and a 0.5 Tesla magnet. The ADC values were higher (hyperintense) in brain metastases according to low-grade astrocytomas. Moseley et al¹⁰ published the first article on the use of DWI to detect acute cerebral ischemia in cats in 1990. Warach et al¹¹ reported

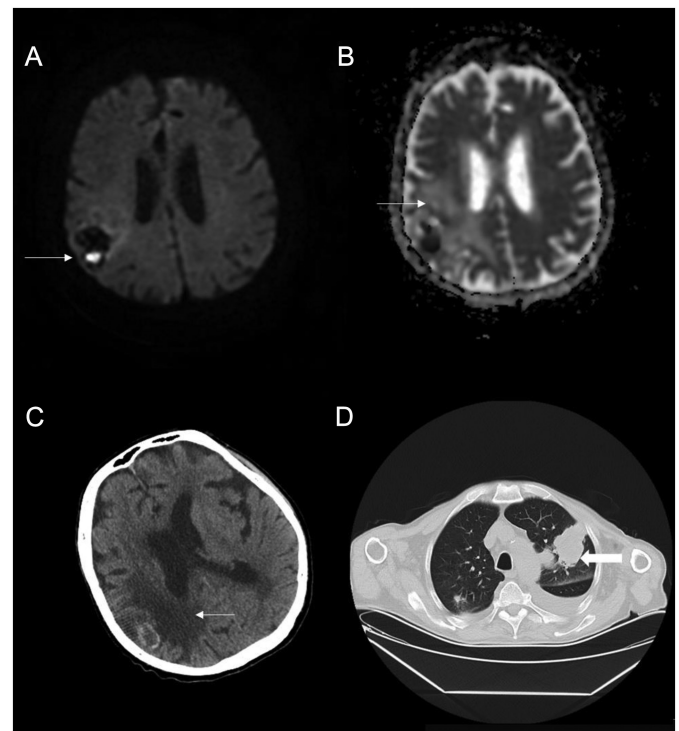


Figure 1. A 70-year-old man with intra-axial gray matter lesion in right parietal lobe. There's a focal diffusion restriction in the posterior aspect of the lesion (A, B) (arrows). Moderate perilesional vasogenic edema is seen (B, C) (arrows). Thorax CT reveals a large mass (arrow) in the upper lobe of left lung (D); pathology results confirm lung cancer in this patient. CT, computed tomography.

MAIN POINTS

- Stroke continues to be one of the primary causes of mortality and morbidity in Western countries.
- Diffusion-weighted imaging (DWI) is a widely utilized magnetic resonance imaging technique that is commonly performed for the evaluation of patients affected by stroke.
- The incidence of brain and other central nervous system tumors in adults aged 20 and above is 31 per 100 000.
- It is crucial to report other radiological findings (especially tumors) besides acute stroke on DWI images and to guide the physician about advanced radiological methods for characterization of lesions.

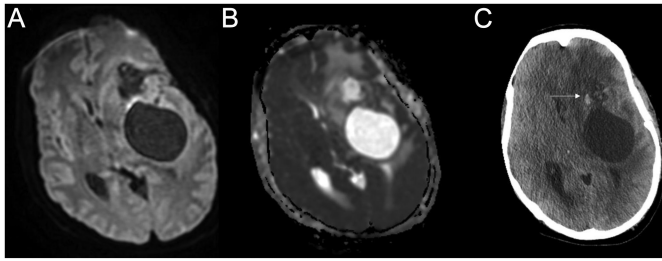


Figure 2. In diffusion-weighted and ADC MR images of a 44-year-old man, a large left temporal cystic/solid lesion with mass effect and compression of the left cerebral peduncle was detected. Solid and hemorrhagic elements on anterior margin (C) (arrow), which do not exhibit restricted diffusion (A, B). Moderate vasogenic edema more pronounced anteriorly. Pathology results confirm GBM in this patient. ADC, apparent diffusion coefficient; GBM, glioblastoma multiforme; MR, magnetic resonance.

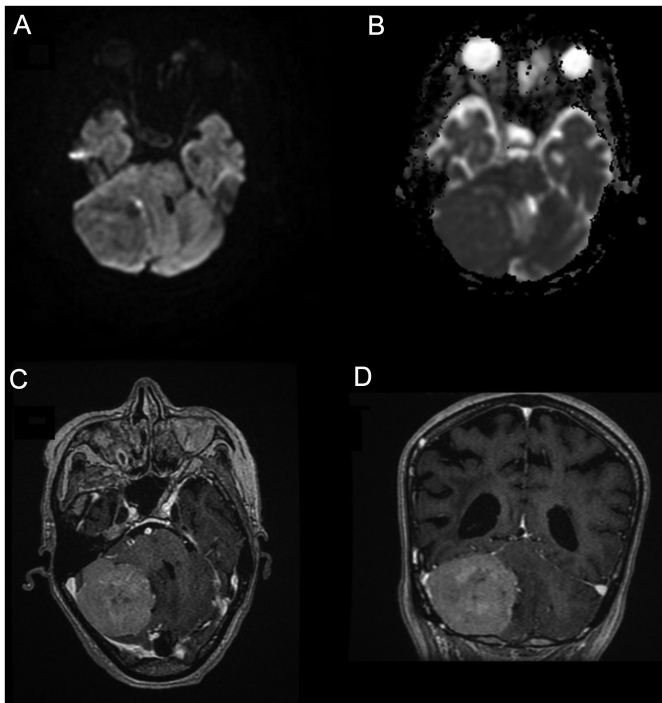


Figure 3. In diffusion-weighted and ADC MR images of a 77-year-old woman, a well-defined extra-axial mass at the right infratentorial region, measuring 5.8 cm × 4.6 cm was detected (A, B). It has a broad base to the dura. The mass also demonstrates homogeneous contrast enhancement (C, D). ADC, apparent diffusion coefficient; MR, magnetic resonance.

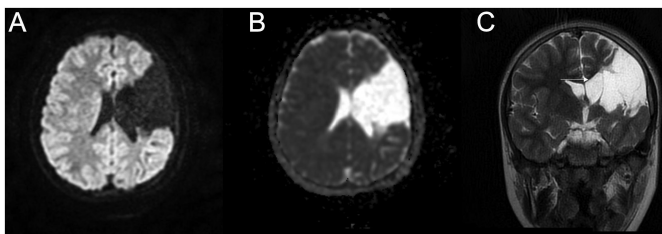


Figure 4. A large porencephalic cyst was detected in the frontotemporal region in diffusion-weighted MR images and ADC map of a 21-year-old man (A, B). Encephalic volume loss in left frontotemporal lobes evidenced by hydrocephalus ex vacuo (C) (arrow). ADC, apparent diffusion coefficient; MR, magnetic resonance.

the first clinical implementation of DWI using a 1.5 T scanner to identify patients with acute stroke in 1992.

The DWI is the most effective technique for detecting ischemic changes within the first few hours following the onset of a stroke.¹²⁻¹⁴ It has been shown to be superior to CT at the acute stage (sensitivity 96.6% vs. 46.9%) and conventional MRI (accuracy 97.5% vs. 64.9%).^{15,16} Therefore, DWI is the first-line radiological imaging method with CT for the evaluation of stroke patients in emergency departments.

Brain tumor patients may present with acute neurologic symptoms that mimic stroke. It is crucial to differentiate brain tumors from strokes as early as possible in order to avoid inappropriate treatments such as thrombolytic therapy, which carries a risk of hemorrhage, and to not delay the brain tumor's management. Magnetic resonance imaging is essential for the initial diagnosis, planning, and monitoring of brain tumors.¹⁷ Using the T2-weighted images, fluid-attenuated inversion recovery, DWI, ADC, and T1-weighted images pre- and post-contrast MRI sequences, brain neoplasms can be readily distinguished from AIS.¹⁸ Brain neoplasms may appear as an ovoid or round-enhancing lesion that is surrounded by vasogenic edema, which are characteristics not observed within the first few hours following the onset of a stroke.^{2,17} However, when brain tumors are small, they may not exhibit all of these characteristics, making it difficult to distinguish them from infarct lesions, especially when they are seen as tumors with restricted diffusion on DWI. Variable signal intensities are exhibited by DWI for both primary and secondary tumors. Cellular density has an inverse proportion with ADC. Consequently, the ADC value of high-grade gliomas is less than that of low-grade gliomas. Similarly, lymphoma typically has a low ADC due to its high cellularity.¹⁷⁻¹⁹

In our study, we observed acute intracranial infarction in 121 patients out of 1544 DWI examinations obtained from the emergency department under suspicion of acute stroke, while 10 patients were diagnosed with intracranial mass. Upon further clinical and radiological evaluation of 3 patients suspected of having brain metastasis, lung cancer was identified in 2 patients and colon cancer in 1 patient. Three patients were diagnosed with meningioma, while 2 patients were diagnosed with GBM. A patient had a porencephalic cyst in the left frontotemporal region. In addition, a patient diagnosed with a cyst in the fourth ventricle was referred to another tertiary care hospital for surgery due to compression of the roof of the fourth ventricle.

Our study has several limitations. First, we do not have the pathology results of all patients because in our study, among the patients in whom a mass was detected, there were patients who did not have an indication for surgery. These patients were subjected to routine clinical and radiological follow-up. Second, we did not investigate age-related variables among patients with infarction and mass detected on diffusion MRI.

In conclusion, while DWI is the first imaging modality used in the evaluation of patients with suspected acute stroke in emergency department, we think that it is crucial to report other radiological findings besides acute stroke on DWI images and to guide the physician about advanced radiological methods for characterization of lesions.

Ethics Committee Approval: Ethics committee approval was received for this study from the ethics committee of Erzincan Binali Yıldırım University (Date: September 7, 2023, Number: kaek-2023-09-01-14572389.E1359002).

Informed Consent: Written informed consent was obtained from patients who participated in this study.

Peer-review: Externally peer-reviewed.

Author Contributions: Concept – E.K., E.T.; Design – E.T.; Supervision – E.K.; Resources – E.T., Ö.Ç.A.; Materials – E.T.; Data Collection and/or Processing – E.T.; Analysis and/or Interpretation – E.T., E.K., B.T.; Literature Search – E.T., Ö.Ç.A.; Writing Manuscript – E.T.; Critical Review – E.K., Ö.Ç.A.; Other – B.T.

Declaration of Interests: The authors declare that they have no competing interest.

Funding: The authors declared that this study has received no financial support.

REFERENCES

1. Zhang XH, Liang HM. Systematic review with network meta-analysis: diagnostic values of ultrasonography, computed tomography, and magnetic resonance imaging in patients with ischemic stroke. *Medicine*. 2019;98(30):e16360. [\[CrossRef\]](#)
2. Adam G, Ferrier M, Patsoura S, et al. Magnetic resonance imaging of arterial stroke mimics: a pictorial review. *Insights Imaging*. 2018;9(5):815-831. [\[CrossRef\]](#)
3. Nagaraja N. Diffusion weighted imaging in acute ischemic stroke: a review of its interpretation pitfalls and advanced diffusion imaging application. *J Neurol Sci*. 2021;425:117435. [\[CrossRef\]](#)
4. Makin SD, Doubal FN, Dennis MS, Wardlaw JM. Clinically confirmed stroke with negative diffusion-weighted imaging magnetic resonance imaging: longitudinal study of clinical outcomes, stroke recurrence, and systematic review. *Stroke*. 2015;46(11):3142-3148. [\[CrossRef\]](#)
5. Merino JG, Luby M, Benson RT, et al. Predictors of acute stroke mimics in 8187 patients referred to a stroke service. *J Stroke Cerebrovasc Dis*. 2013;22(8):e397-e403. [\[CrossRef\]](#)
6. Louis DN, Perry A, Wesseling P, et al. The 2021 WHO Classification of Tumors of the central nervous system: a summary. *Neuro-Oncology*. 2021;23(8):1231-1251. [\[CrossRef\]](#)
7. Ostrom QT, Francis SS, Barnholtz-Sloan JS. Epidemiology of brain and other CNS tumors. *Curr Neurol Neurosci Rep*. 2021;21(12):68. [\[CrossRef\]](#)
8. Ostrom QT, Patil N, Cioffi G, Waite K, Kruchko C, Barnholtz-Sloan JS. CBTRUS statistical report: primary brain and other central nervous system tumors diagnosed in the United States in 2013-2017. *Neuro-Oncology*. 2020;22(12 suppl 2):iv1-iv96. [\[CrossRef\]](#)
9. Le Bihan D, Breton E, Lallemand D, Grenier P, Cabanis E, Laval-Jeantet M. MR imaging of intravoxel incoherent motions: application to diffusion and perfusion in neurologic disorders. *Radiology*. 1986;161(2):401-407. [\[CrossRef\]](#)
10. Moseley ME, Cohen Y, Mintorovitch J, et al. Early detection of regional cerebral ischemia in cats: comparison of diffusion- and T2-weighted MRI and spectroscopy. *Magn Reson Med*. 1990;14(2):330-346. [\[CrossRef\]](#)
11. Warach S, Chien D, Li W, Ronthal M, Edelman RR. Fast magnetic resonance diffusion-weighted imaging of acute human stroke. *Neurology*. 1992;42(9):1717-1723. [\[CrossRef\]](#)
12. Lövgren KO, Laubach HJ, Baird AE, et al. Clinical experience with diffusion-weighted MR in patients with acute stroke. *AJNR Am J Neuroradiol*. 1998;19(6):1061-1066.
13. Chen PE, Simon JE, Hill MD, et al. Acute ischemic stroke: accuracy of diffusion-weighted MR imaging--effects of b value and cerebrospinal fluid suppression. *Radiology*. 2006;238(1):232-239. [\[CrossRef\]](#)
14. González RG, Schaefer PW, Buonanno FS, et al. Diffusion-weighted MR imaging: diagnostic accuracy in patients imaged within 6 hours of stroke symptom onset. *Radiology*. 1999;210(1):155-162. [\[CrossRef\]](#)
15. Chalela JA, Kidwell CS, Nentwich LM, et al. Magnetic resonance imaging and computed tomography in emergency assessment of patients with suspected acute stroke: a prospective comparison. *Lancet*. 2007;369(9558):293-298. [\[CrossRef\]](#)
16. Davis DP, Robertson T, Imbesi SG. Diffusion-weighted magnetic resonance imaging versus computed tomography in the diagnosis of acute ischemic stroke. *J Emerg Med*. 2006;31(3):269-277. [\[CrossRef\]](#)
17. Morgenstern LB, Frankowski RF. Brain tumor masquerading as stroke. *J Neurooncol*. 1999;44(1):47-52. [\[CrossRef\]](#)
18. Yang D, Korogi Y, Sugahara T, et al. Cerebral gliomas: prospective comparison of multivoxel 2D chemical-shift imaging proton MR spectroscopy, echoplanar perfusion and diffusion-weighted MRI. *Neuroradiology*. 2002;44(8):656-666. [\[CrossRef\]](#)
19. Law M, Yang S, Wang H, et al. Glioma grading: sensitivity, specificity, and predictive values of perfusion MR imaging and proton MR spectroscopic imaging compared with conventional MR imaging. *AJNR Am J Neuroradiol*. 2003;24(10):1989-1998.

The Role of Multiparametric Scrotal Magnetic Resonance Imaging in the Histological Differentiation of Germ Cell Neoplasia In Situ-Related Testicular Germ Cell Tumors: Can Seminomatous and Mixed-Non-Seminomatous Germ Cell Tumors Be Separated?

Serdar Aslan¹ , Uluhan Eryürük¹ , Ural Oğuz² , İsmet Miraç Çakır^{1,3} 

¹Department of Radiology, Giresun University Faculty of Medicine, Giresun, Turkey

²Department of Urology, Giresun University Faculty of Medicine, Giresun, Turkey

³Department of Radiology, Samsun Education and Research Hospital, Samsun, Turkey

Cite this article as: Aslan S, Eryürük U, Oğuz U, Çakır İM. The role of multiparametric scrotal Magnetic Resonance Imaging in the histological differentiation of germ cell neoplasia insitu-related testicular germ cell tumors: Can seminomatous and mixed-non-seminomatous germ cell tumors be separated? *Current Research in MRI* 2023;2(3):63-69.

Corresponding author: Uluhan Eryürük, e-mail: uluhaneryuruk@gmail.com

Received: September 27, 2023 **Accepted:** October 15, 2023 **Publication Date:** October 30, 2023

DOI:10.5152/CurrResMRI.2023.23078



Content of this journal is licensed under a Creative Commons Attribution-NonCommercial 4.0 International License.

Abstract

Objective: The aim was to examine the efficacy of multiparametric magnetic resonance imaging (mp-MRI) in the histological differentiation of germ cell neoplasia in situ (GCNIS)-related testicular germ cell tumors (TGCTs).

Methods: We retrospectively included 58 patients with histologically proven GCNIS-related TGCTs, who underwent mp-MRI between November 2019 and June 2022. The signal characteristics of the tumors on T2-weighted imaging were recorded. The mean apparent diffusion coefficient (ADC) values were calculated. Time signal intensity curves were generated, and semiquantitative parameters were calculated. The presence of a septal enhancement pattern within the tumor was noted. Receiver operating characteristic curve analysis was performed to assess the diagnostic performance of the parameters.

Results: Histopathological examination revealed that 24 of the cases were seminomas, and 10 were non-seminomatous GCT (NSGCTs). The incidence of hypointense signals was notably higher for seminomas ($P < .001$). The mean ADC values of the seminomas were lower than NSGCTs (0.645 ± 0.11 and 0.879 ± 0.061 , respectively, $P < .001$). The optimal ADC cutoff value was $0.779 \times 10^{-3} \text{ mm}^2/\text{s}$. No differences were observed between the 2 groups for semiquantitative parameters ($P = .16-.83$). However, the septal enhancement pattern was more frequent in seminomas ($P = .002$).

Conclusion: Values of ADC measured in mp-MRI can be used as a reliable preoperative method in the histological differentiation of GCNIS-related TGCTs. Also, the septal enhancement pattern can be helpful in distinguishing between seminoma and NSGCT.

Keywords: Germ cell neoplasia in situ-related testicular germ cell tumors, magnetic resonance imaging, apparent diffusion coefficient, dynamic contrast-enhanced imaging, differential diagnosis

INTRODUCTION

Testicular cancer (TC) represents approximately 1% of male neoplasms.¹ However, it represents the most common type of cancer in the male demographic aged 15-35 years, contributing to approximately 10%-14% of cancer cases in this age group.^{1,2} It is estimated by the American Cancer Society that in 2022, 9910 men will develop TC, and 460 men will die from this disease.³ Most TCs are testicular germ cell tumors (TGCTs) originating from the germinal epithelium of the seminiferous tubules.^{4,5} The TGCTs are divided into 2 groups: germ cell neoplasia in situ (GCNIS)-related TGCTs and non-GCNIS-related TGCTs. The GCNIS-related TGCTs are also divided into 3 groups: seminomas, mixed-non-seminomatous GCT (NSGCT), and burned-out GCTs. Seminomas and mixed-NSGCT constitute the majority of GCNIS-related TGCTs.⁶ The general morphology and histological features of these 2 broad tumor groups differ from each other, and it is emphasized that this situation is related to imaging features.⁷⁻¹⁰

Radical orchiectomy is the preferred therapeutic approach for cases of TGCTs associated with GCNIS and should be carried out promptly unless clinical circumstances necessitate immediate chemotherapy.¹¹ In these cases, a noninvasive imaging modality would be of great benefit to help predict the histological characteristics of GCNIS-related TGCTs preoperatively.

Currently, ultrasonography (US) is accepted as the first choice for the diagnostic imaging of testicular masses.¹²⁻¹⁴ However, changes in echogenicity may not be specific, and reliable characterization of testicular masses is not always possible.¹⁵⁻¹⁹

Recently, it has been shown that magnetic resonance imaging (MRI) shows high diagnostic performance for both morphological evaluation and tissue characterization in testicular masses.^{8-10,15,17-19} The benefits of this technique encompass concurrent multi-plane imaging of both testes and paratesticular areas, providing high contrast and spatial resolution, offering satisfactory anatomical and functional information, with no radiation exposure, and exhibiting reduced reliance on the operator when contrasted with US.^{14,18,20} Previous studies showed that conventional MRI features of GCNIS-related TGCTs are closely related to histological features and that diffusion-weighted images (DWIs) and dynamic contrast-enhanced (DCE) images play an important role in the characterization of scrotal masses.^{7-9,17-19,21,22} However, all of these studies separately compared the MRI features of GCNIS-related TGCTs with histological features.

To the best of our knowledge, there is no study that correlates multiparametric magnetic resonance imaging (mp-MRI) findings with histological features. Our aim in this study is to investigate the efficacy of mp-MRI in distinguishing between seminoma and mixed-NSGCT.

METHODS

Approval for this retrospective study was granted by the Institutional Ethics Committee (Ethics Committee number: KAEK-108, date: March 18, 2021, Giresun University). Given its retrospective nature, necessity for informed consent was waived.

Study Population

A search of our institutional electronic medical database was performed to identify patients who met the specified inclusion criteria for the period spanning from November 2019 to June 2022: patients who (1) had histopathological evidence of GCNIS-related TGCTs after radical orchiectomy and (2) underwent an mp-MRI scan. The exclusion criteria included (1) unsatisfactory image quality and (2) mainly hemorrhagic and/or necrotic tumors. In the case of bilateral tumors, each tumor was evaluated separately. The final study population comprised 30 patients with 34 tumors. The mean time between the MRI examination and radical orchiectomy was 2.7 days. Patient selection is shown in Figure 1.

Magnetic Resonance Imaging Protocol

All MRI examinations were carried out using a 1.5-T MRI system (Magnetom Symphony, Siemens Medical Solutions, Erlangen, Germany) with a circular surface coil. Patients were examined in a supine position, with the testicles placed equidistant from the coil, utilizing a cloth placed beneath them, and with the penis resting on the lower abdominal wall. The MRI protocol consisted of the following

sequences: unenhanced axial T1-weighted image (T1-WI), 3 planes (axial, coronal, and sagittal) T2-WI, axial DWI with *b*-values of 0, 400, and 800 s/mm², DCE images with 3-dimensional (3D) high temporal resolution. Gadopentetate dimeglumine (Gadovist, 0.2 mL per kilogram of body weight; Bayer Healthcare, Berlin, Germany) was introduced at a rate of 2 mL per second utilizing a power injector, succeeded by a subsequent infusion of 20 mL of normal saline. After IV contrast material injection, axial DCE images were obtained in 7 postcontrast phases with no interval between them. Also, coronal DCE images were obtained after injection. Table 1 details the technical parameters of the MRI sequences.

Magnetic Resonance Image Analysis

The MR images of 30 patients with 34 GCNIS-related TGCTs were transferred to a picture archiving communication system (PACS). The MRI data were interpreted in consensus by 2 radiologists (board-certified urogenital radiologist with >10 years of experience and a general radiologist with 8 years of experience, respectively). All radiologists were blinded to the histological data of the patients. Signal characteristics of the tumors on T2-WI were recorded, and the longest diameter (LD) was measured.

The DWI was evaluated with reference to axial T2-WI. Apparent diffusion coefficient (ADC) maps—were generated based on the high *b*-value DWI. For quantitative analysis, a circular region of interest (ROI) was defined as wide as possible within the tumor. The ROIs were meticulously drawn to omit artifacts and regions with hemorrhaging and/or necrosis, assisted by T1-WI, T2-WI, and DCE images. Tumor presence on ADC maps was defined as areas with low signal intensity (SI). Three measurements were made on the ADC maps, and the average was taken.

The enhancement patterns of tumors were evaluated on the maximum enhanced image and classified as heterogeneous or homogeneous. In addition, it was recorded whether there was a septal enhancement pattern within the tumor. The ROIs were placed in areas of tumors that showed maximum enhancement with care and with the aid of the corresponding T1- and T2-WI to exclude areas of hemorrhage and necrosis. Time SI (TSI) curves of the measured MRI signal for each ROI in arbitrary units plotted against time in seconds were compiled. The enhancement pattern was classified into 1 of 3 types according to the shape of the TSI curves: type I, a linear increase in enhancement over the entire dynamic period; type II, an initial upstroke followed by a plateau or mild-gradually increased; and type III, an initial upstroke followed by gradual washout. The TSI curves of all tumors were recorded. In addition, the measured SI from tumors (S_i ($i = 0, 1, \dots, 7$)) were normalized according to the formula $(S_i - S_0) / S_0$ with the help of precontrast SI (S_0). The following parameters first described by Tsili et al⁸ were calculated using normalized measurements:

- Peak enhancement (PE) is described as the maximum S_i of the tumor.
- Time to peak (TTP) is described as the time to reach the maximum S_i of the tumor.
- Wash-in rate (WIR) is described as the maximum slope of tumor enhancement before TTP and calculated by the following formula; $WIR = \max S_i (PE) - S_{i-1} / \max t_i - t_{i-1}$
- Wash-out rate (WOR) is described as $\max S_i (PE) - S_7$, i.e., the difference between the maximum signal and the signal at the last time point.

MAIN POINTS

- Accurate characterization of testicular masses during the preoperative period is very important.
- Multiparametric magnetic resonance imaging can be used as a reliable preoperative method in the histological differentiation of germ cell neoplasia in situ-related testicular germ cell tumors.
- Reduced apparent diffusion coefficient values, low signal on T2-weighted imaging, and a septal enhancement pattern with high intensity in contrast to the tumor are imaging characteristics indicative of seminomas.
- Dynamic contrast-enhanced images have no proven role in the seminoma–non-seminomatous germ cell tumor distinction.

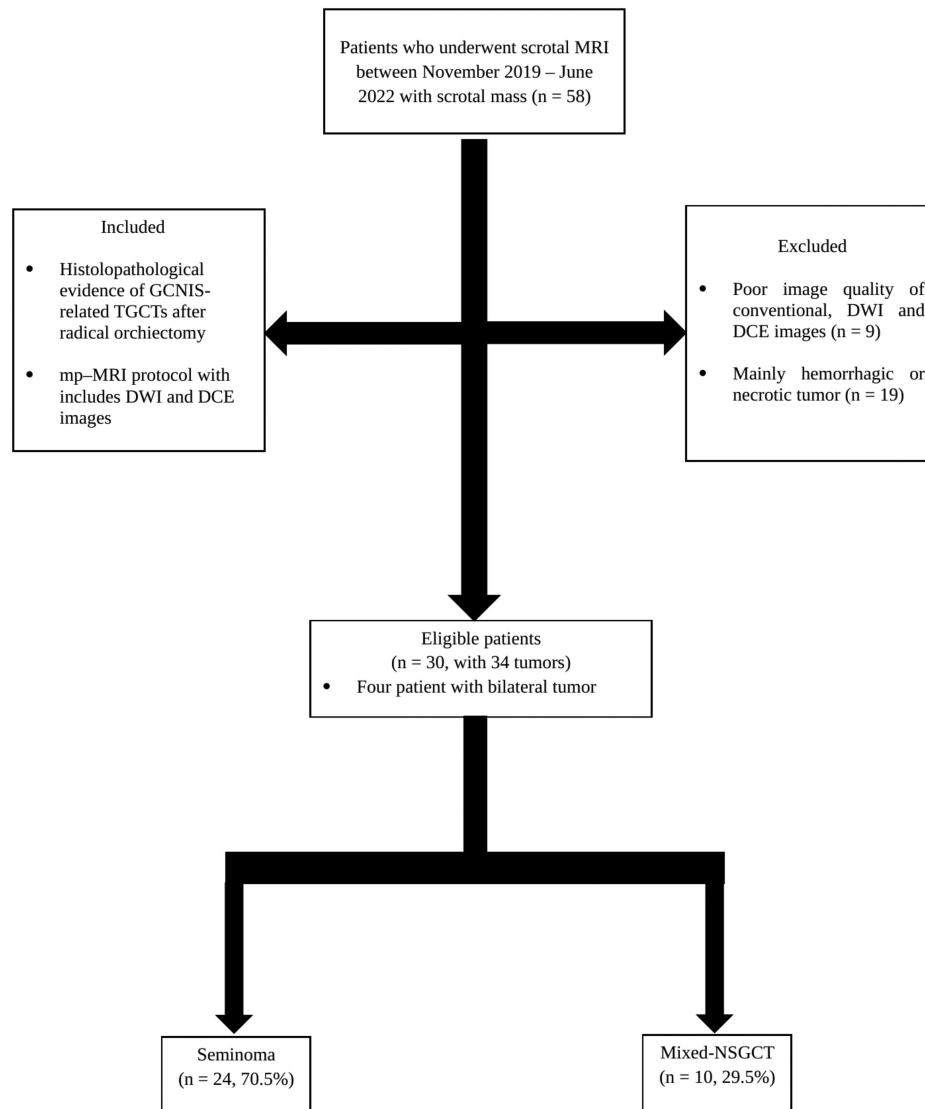


Figure 1. Flowchart of patient selection.

DCE, dynamic contrast-enhanced images; DWI, diffusion-weighted images; GCNIS, germ cell neoplasia in situ; MRI, magnetic resonance imaging; TGCT, testicular germ cell tumor.

Standard of Reference

A standard procedure of radical orchiectomy was performed for all tumors, with evaluation carried out by a pathologist possessing 15 years of expertise in the field of uropathology. The World Health Organization-2016 classification of TGCTs was used to classify the tumors. The pathologist was blinded to the mp-MRI findings during the evaluation.

Statistical Analysis

Statistical analyses were conducted using IBM Statistical Package for the Social Sciences Statistics software, version 25 (IBM SPSS Corp., Armonk, NY, USA). The assessment of data normality was carried out with the Kolmogorov–Smirnov test, and for normally distributed quantitative data, mean values were presented along with their corresponding SDs. Categorical variables were presented as numbers and percentages. The Mann–Whitney *U*-test was used to compare the mean values of ADC, PE, TTP, WIR, and WOR, and the LD between seminomas and mixed-NSGCTs. Receiver operating characteristic

(ROC) curve analysis was performed to assess the diagnostic performance of parameters displaying distinct mean values between the 2 tumor groups. Statistical calculations were performed using 95% CIs. A *P*-value < .05 was considered statistically significant.

RESULTS

The study included 30 patients with 34 GCNIS-related TGCTs (mean \pm SD, 35.2 ± 14.6 years; range, 26–89). In the study, 4 patients had bilateral tumors. Of the 34 GCNIS-related TGCTs, 24 (70.5%) were seminomas, and 10 (29.5%) were mixed-NSGCTs. Of the 10 mixed-NSGCTs, 4 (40%) were embryonal carcinoma and postpubertal teratoma, 2 (20%) were embryonal carcinoma, 2 (20%) were postpubertal yolk sac tumor, embryonal carcinoma, and postpubertal teratoma, and 2 (20%) were postpubertal yolk sac tumor and embryonal carcinoma.

The LDs were measured as 4.3 ± 2.4 cm and 3.6 ± 2.1 cm in seminoma and mixed-NSGCT cases, respectively. There was no significant difference between the 2 groups (*P* = .467). Twenty-four (20 seminomas and

Table 1. Technical Details of Multiparametric Magnetic Resonance Imaging Scanning Parameters

	T2-WI	T1-WI	DWI	DCE
Imaging planes	Axial, coronal, sagittal	Axial	Axial	Axial
Fat saturation	-	-	-	Fat-sat
Sequence	TSE	GRE	EPI	3D GRE
TE (ms)	100	15	110	4.1
TR (ms)	4000	500	4000	9
Flip angle (degrees)	90	90	90	35
NEX	2	1	12	1
FOV (cm)	24	24	24	22
Slice thickness	3	3	3	3
Matrix size	180 × 256	240 × 270	180 × 256	256 × 256
<i>b</i> value (s/mm ²)	-	-	0, 400, 800	-
Temporal resolution (s)	-	-	-	45
Number of acquisitions	-	-	-	7

DWI sequences included ADC map calculation.

ADC, apparent diffusion coefficient; DCE, dynamic contrast-enhanced images; DWI, diffusion-weighted images; EPI, Echo planar imaging; Fat-sat, fat saturated; FOV, field of view; GRE, Gradient recall echo; NEX, number of excitation; TE, time to echo; TR, time to repetition; TSE, Turbo spin echo; T1-WI, T1-weighted images; T2-WI, T2-weighted images.

4 mixed-NSGCTs) of the tumors were hypointense and 10 (4 seminomas and 6 mixed-NSGCTs) were isointense on T2-WI. Hypointense signal on T2-WI was statistically significant for seminomas compared to mixed-NSGCT ($P < .001$).

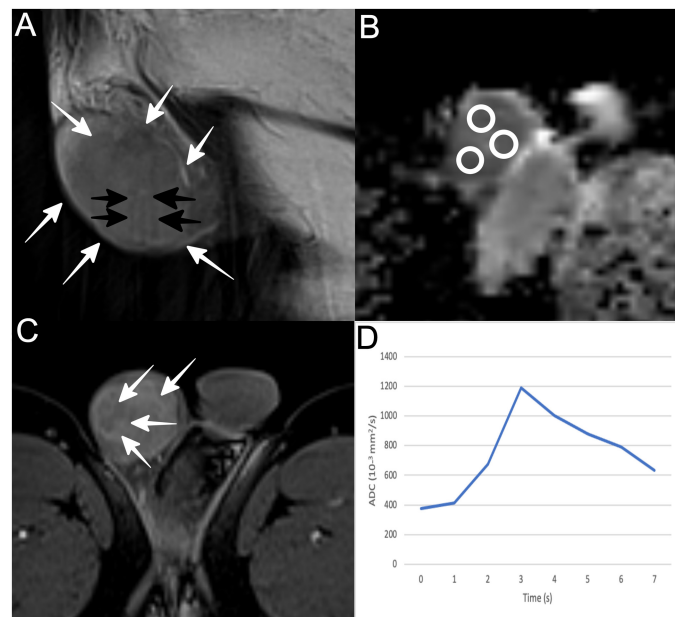


Figure 2. Right testicular seminoma in a 23-year-old man. (A) Sagittal T2-weighted image shows hypointense right testicular mass (white arrows). Tumor septa are also seen as hypointense bands (black arrows). (B) Axial ADC map ($b = 800 \text{ s/mm}^2$) shows tumor's restricted diffusion. The mean ADC values of tumor (circular ROIs) were $0.49 \times 10^{-3} \text{ mm}^2/\text{s}$. (C) Axial DCE image at early phase (180 seconds) shows heterogeneous tumor enhancement. Septal enhancement (arrows) more than the remaining tumoral tissue. (D) TSI curve shows early tumor enhancement, followed by gradual washout in the delayed phase (type III).
ADC, apparent diffusion coefficient; DCE, dynamic contrast-enhanced images; ROI, region of interest; TSI, time signal intensity.

On DWI, all tumors showed restricted diffusion compared to normal testicular parenchyma (Figures 2, 3 and 4). The mean ADC values of the seminomas were statistically significantly lower than those of the mixed-NSGCTs (0.645 ± 0.11 and 0.879 ± 0.061 , respectively, $P < .001$). Figure 5 clearly shows the difference between ADC value box plots for seminoma and mixed-NSGCTs. In the ROC curve analysis for ADC values, the area under the curve for the differentiation of seminoma and mixed-NSGCT was 0.983 (Figure 6). The optimal ADC cutoff point that simultaneously maximized sensitivity (91.6%), specificity (100%), and accuracy (94.1%) was $0.779 \times 10^{-3} \text{ mm}^2/\text{s}$.

All tumors showed a type III TSI curve (Figures 2D, 3D, and 4D). In 14 (58.3%) of 24 seminomas, more intensely enhanced septa were observed compared to solid tumor areas (Figure 2C and 3C), whereas no enhanced septa was observed in any of the mixed-NSGCTs (Figure 4C) ($P = .002$). Table 2 presents the mean values of PE, TTP, WIR, and WOR for seminoma and mixed-NSGCT. There was no significant difference between the 2 groups for PE, TTP, WIR, and WOR ($P = .21, .83, .31, \text{ and } .16$, respectively).

DISCUSSION

The results of our study showed that the measurement of ADC values, based on high *b*-value DWI, can largely distinguish between seminomas and mixed-NSGCTs since the cutoff value of $0.779 \times 10^{-3} \text{ mm}^2/\text{s}$ is used. Our results are similar to those previously reported in the literature.^{9,10,23,24} In addition, in our study, DCE images showed the presence of septa with more intense enhancement compared to tumor tissue in most of the seminoma (58.3%), but this finding was not observed

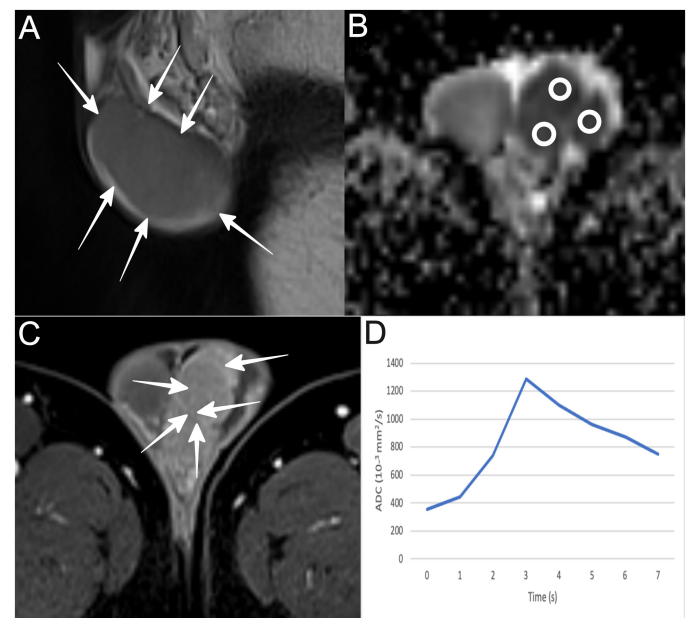


Figure 3. Left testicular seminoma in a 55-year-old man. (A) Sagittal T2-weighted image shows large hypointense left testicular mass (arrows), replacing the ipsilateral testis. (B) Axial ADC map ($b = 800 \text{ s/mm}^2$) shows tumor's restricted diffusion. The mean ADC values of tumor (circular ROIs) were $0.53 \times 10^{-3} \text{ mm}^2/\text{s}$. (C) Axial DCE image at early phase (180 seconds) shows heterogeneous tumor enhancement. Septal enhancement (arrows) more than the remaining tumoral tissue. (D) TSI curve is typical of malignancy (type III).
ADC, apparent diffusion coefficient; DCE, dynamic contrast-enhanced images; ROI, region of interest; TSI, time signal intensity.

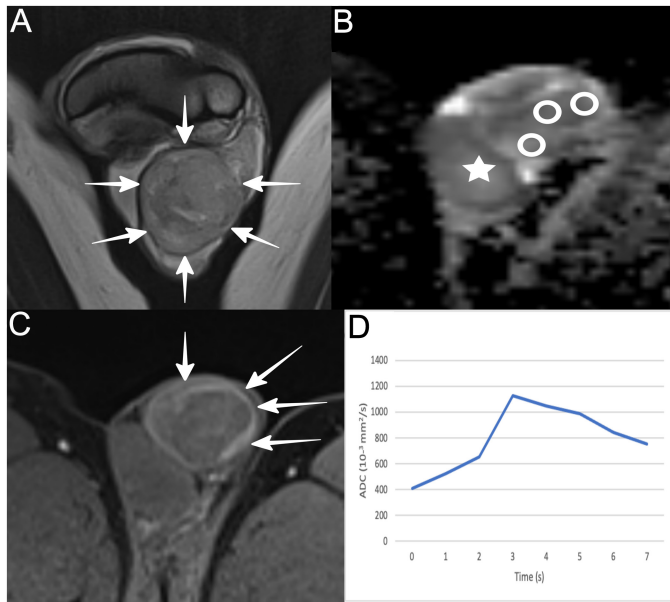


Figure 4. Left mixed-NSGCT (postpubertal type yolk sac, embryonal carcinoma, and postpubertal type teratoma) in a 31-year-old man. (A) Coronal T2-weighted image shows large heterogeneous hypointense left testicular mass (arrows). (B) Axial ADC map ($b=800 \text{ s/mm}^2$) shows the tumor appears slightly hypointense compared to the contralateral testis (star) and has mild restricted diffusion. The mean ADC values (circular ROIs) of the tumor were $1.07 \times 10^{-3} \text{ mm}^2/\text{s}$. (C) Axial DCE image in the early phase (180 seconds) shows nonhomogeneous circumferential tumor enhancement (arrows). Septal enhancement is absent. (D) TSI curve is typical of malignancy (type III). ADC, apparent diffusion coefficient; DCE, dynamic contrast-enhanced images; NSGCT, non-seminomatous germ cell tumor; ROI, region of interest; TSI, time signal intensity.

in mixed-NSGCTs. This result is also similar to those previously reported by Tsili et al,⁹ and the septal contrast enhancement pattern on DCE images suggests that it can be used to differentiate between seminoma and mixed-NSGCT. Also, we revealed that the majority of seminomas had a hypointense signal on T2-WI, and the presence of a hypointense signal on T2-WI was higher in seminomas compared to

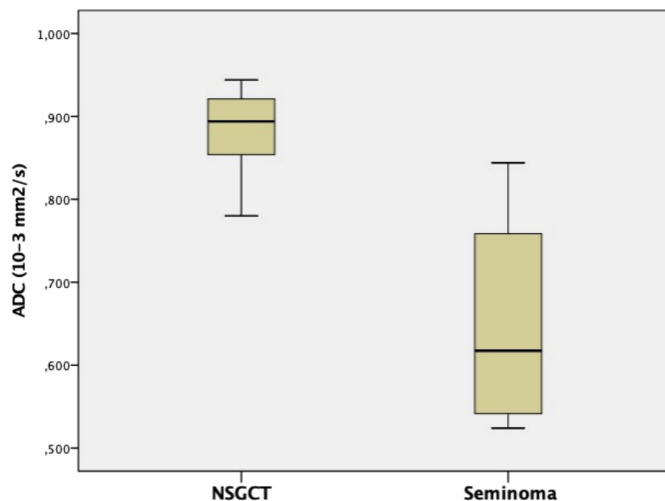


Figure 5. Box plots showing differences of ADC values between seminomas and mixed-NSGCT. ADC, apparent diffusion coefficient; NSGCT, non-seminomatous germ cell tumor.

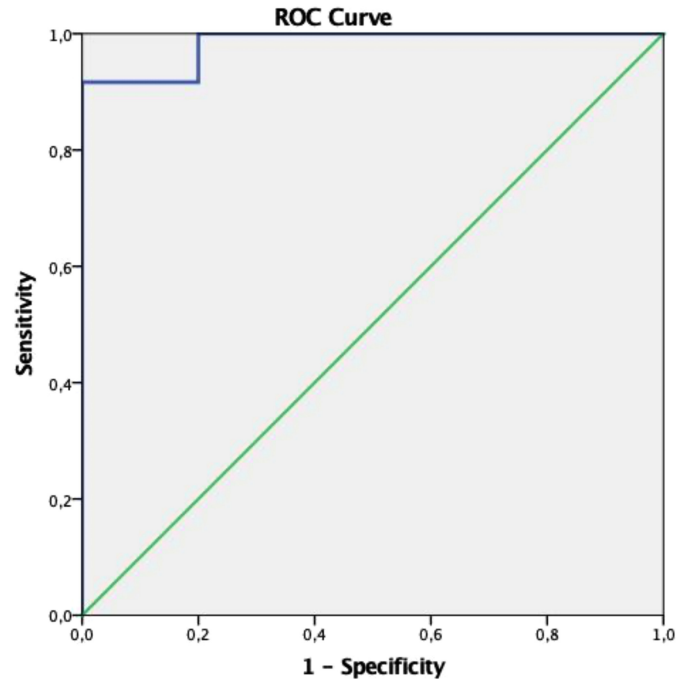


Figure 6. Receiver operating characteristic curve demonstrating the diagnostic performance of ADC values in differentiating seminomas from mixed-NSGCT. ADC, apparent diffusion coefficient; NSGCT, non-seminomatous germ cell tumor; ROC, receiver operating characteristic curve.

mixed-NSGCTs ($P < .001$). This result was in parallel with studies that showed a close relationship between morphological imaging parameters and histological features of GCNIS-related TGCTs.^{7,8}

As is known, radical orchiectomy is the preferred method for the treatment of GCNIS-related TGCTs and should be performed without delay. Nonetheless, in situations involving extensive disease and/or metastases that pose an immediate threat to life, emergency chemotherapy is warranted. Orchiectomy may be postponed until clinical stabilization has been attained.¹ It is very important to perform the histological characterization of GCNIS-related TGCTs with a non-invasive method in these cases.

More recently, morphological MRI sequences were found to be closely related to the histological features of GCNIS-related TGCTs.⁷⁻¹⁰ Tsili et al⁸ reported that 19 of 21 TGCTs were correctly classified preoperatively as seminoma or mixed-NSGCT in their study based on morphological MRI features. In our study, we showed that the T2-WI hypointense signal characteristic was identified with seminomas and was higher than mixed-NSGCTs ($P < .001$), similar to Tsili et al.⁸ We think that this is due to the histological features of seminomas, which

Table 2. Mean Values of Relative Time Signal Intensity Parameters for Seminomas and Mixed-Non-Seminomatous Germ Cell Tumor

TSI Parameter	Seminoma (n=24)	Mixed-NSGCT (n=10)	P
PE	2.18 ± 0.87	3.08 ± 0.98	.21
TTP	4.18 ± 0.68	4.21 ± 0.75	.83
WIR	1.96 ± 0.64	2.02 ± 0.88	.31
WOR	0.18 ± 0.58	0.11 ± 0.51	.16

NSGCT, non-seminomatous germ cell tumor; PE, peak enhancement; TSI, time signal intensity; TTP, time to peak; WIR, wash-in rate; WOR, wash-out rate.

consist of a uniform population of large cells arranged in the lobules and cords. On the other hand, we think that mixed-NSGCTs have a more heterogeneous appearance compared to seminomas in morphological MRI parameters, due to the fact that they represent a large group consisting of different tumors and the higher frequency of necrosis.^{5,7,9}

In our study, we performed ADC measurements based on high *b*-value DWI to distinguish between seminoma and mixed-NSGCT. Our results showed that ADC values were lower in seminomas compared to mixed-NSGCTs (0.645 ± 0.11 and 0.879 ± 0.061 , respectively, $P < .001$). In addition, our results showed that seminoma-mixed-NSGCT discrimination can be made with high sensitivity, specificity, and accuracy when $0.779 \times 10^{-3} \text{ mm}^2/\text{s}$ is used as the optimal ADC cutoff value. Tsili et al⁹ reported that the ADC values of seminomas were lower than those of mixed-NSGCT (0.59 ± 0.009 and 0.90 ± 0.33 , respectively, $P < .001$) and showed that a seminoma-mixed-NSGCT distinction is possible with an optimal cutoff point of $0.68 \times 10^{-3} \text{ mm}^2/\text{s}$ for ADC values. Our results were similar to those previously reported in the literature. The diffusion restriction and low ADC values seen in seminomas are interpreted as secondary to the restriction of the mobility of water molecules due to histological features, such as the presence of large cells with abundant cytoplasm and large nuclei surrounded by fibrous trabeculae and accompanying lymphocyte infiltrates, plasma cells, eosinophils, and granulomatous reactions.^{5,9,10}

While measuring ADC values in our study, we used a circular ROI by avoiding areas of necrosis and hemorrhage, and we took the average value by making 3 measurements from different areas of the tumor. There are limited studies in the literature regarding ROI-drawing techniques in the differentiation of GCNIS-related TGCTs. In the study of Tsili et al,¹⁰ the use of multiple and circular ROIs and the calculation of the mean ADC value have been presented as the most useful methods in the histological characterization of GCNIS-related TGCT. It has been reported that the use of circular and multiple ROIs and obtaining average ADC values give more appropriate and accurate results in studies conducted for the differentiation of different testicular tumor groups for ADC measurement.^{25,26} The results previously reported in the literature are similar to our study and show the accuracy of the ADC measurement results used in our study. We think that it is important to use multiple and circular ROIs when measuring ADC values to prevent possible false results due to the frequent occurrence of necrosis and hemorrhage, especially in mixed-NSGCTs, in the differentiation of GCNIS-related TGCTs.

In our study, a type III TSI curve was seen in DCE images in both seminoma and mixed-NSGCT cases. As is known, lesions with a type III TSI curve have a high PPV for the diagnosis of malignancy.^{18,21,27-29} Previous studies by Tsili et al^{9,22} reported that testicular tumors had a type III TSI curve. The type III TSI curve seen in tumors is thought to result from increased angiogenesis of the tumor, increased intratumoral arteriovenous shunts, and highly permeable vascular structures.²⁷⁻³² Further studies are needed to determine the utility of the type III TSI curve in distinguishing testicular tumors from benign processes. However, we believe that the TSI curves have no benefit for the histological differentiation of GCNIS-related TGCTs.

In our study, we also calculated 4 parameters from the TSI curves: PE, TTP, WIR, and WOR. We found that none of these parameters was statistically significant in the distinction between seminoma and mixed-NSGCT ($P = .21, .83, .31$, and $.16$, respectively). In previous

studies, Tsili et al⁹ reported that PE, TTP, WIR, and WOR parameters did not differ in the distinction between seminoma and mixed-NSGCT ($P = .18, .63, .32$, and $.18$, respectively), which is similar to our results. Tsili et al²¹ reported in another study that only the relative maximum time (representing TTP) differed significantly between benign and malignant tumors ($P < .001$). As commonly recognized, tumor vascularity exhibits several characteristics linked to malignancies, such as spatial heterogeneity, disorganized structure, arteriovenous shunts, elevated vascular tortuosity and vasodilation, and the existence of inadequately developed fragile vessels featuring heightened permeability owing to the existence of large endothelial space cells.^{9,27-29} We think that DCE images can be used in the differentiation of benign and malignant testicular masses because they are based on vascular patterns; however, they are not suitable for histological differentiation of GCNIS-related TGCTs because both seminomas and mixed-NSGCTs share the abovementioned features. However, we think that the septal contrast enhancement pattern, which we detected only in seminomas in our study, may help DCE images to distinguish between seminoma and mixed-NSGCT.

This study has some limitations. First, although it is the largest patient group in the literature to the best of our knowledge, it is a retrospective study conducted with a relatively small group of patients. In addition, mixed-NSGCTs represent a highly heterogeneous group, and the mp-MRI features of different histological subtypes may differ. Therefore, we think that multicenter studies with large patient populations are needed to perform histological characterization of GCNIS-related TGCTs in the preoperative period. Second, in our study, we did not use the whole tumor volume ROI for ADC measurements; we measured from 3 different points and averaged them. Although the whole tumor volume ROI is considered a reliable method, it is time-consuming and difficult to use in routine clinical practice. Third, MRI data were interpreted in consensus by the 2 radiologists; therefore, interobserver reliability was not assessed. Finally, we consider it possible that our findings could exhibit variations between and within scanners. This variability can be attributed to the significant differences in ADC measurements stemming from diverse factors, such as the types of coils, imagers, suppliers, and magnetic field strengths used for MRI. Despite these limitations, our study is the first to evaluate the histological differentiation of GCNIS-related TGCTs preoperatively using mp-MRI. We think that it will be a pioneer among the studies to be done on this subject.

Our study shows that mp-MRI including morphological images and ADC values, can be used as a reliable preoperative method in the histological differentiation of GCNIS-related TGCTs. The semiquantitative parameters obtained from DCE images have proven to be not specific enough to allow histological characterization of GCNIS-related TGCTs. Only the septal enhancement pattern on DCE images can be helpful in distinguishing between seminoma and mixed-NSGCT. Although histopathological examination remains the gold standard for the characterization of GCNIS-related TGCTs, larger prospective studies will help demonstrate the potential role of mp-MRI as a non-invasive method as an aid in the histological differentiation of these tumors.

Ethics Committee Approval: Ethics committee approval was received for this study from the ethics committee of Giresun University (Date: March 18, 2021, Number: KAEK-108).

Informed Consent: Due to its retrospective design, we waived the requirement for informed consent.

Peer-review: Externally peer-reviewed.

Author Contributions: Concept – S.A.; Design – S.A.; Supervision – U.O.; Materials – S.A., U.O.; Data Collection and/or Processing – S.A., U.E.; Analysis and/or Interpretation – İ.M.Ç.; Literature Search – U.E.; Writing Manuscript – S.A., U.E., İ.M.Ç.; Critical Review – U.O.

Declaration of Interests: The authors declare that they have no conflict of interest.

Funding: The authors declared that this study has received no financial support.

REFERENCES

1. Albers P, Albrecht W, Algaba F, et al. Guidelines on testicular cancer: 2015 update. *Eur Urol*. 2015;68(6):1054-1068. [\[CrossRef\]](#)
2. Yacoub JH, Oto A, Allen BC, et al. ACR appropriateness criteria staging of testicular malignancy. *J Am Coll Radiol*. 2016;13(10):1203-1209. [\[CrossRef\]](#)
3. American Cancer Society. Cancer facts & figures 2022. Available at: <https://www.cancer.org/content/dam/cancer-org/research/cancer-facts-and-statistics/annual-cancer-facts-and-figures/2022/cancerfacts-and-figures-2022.pdf>. Accessed 13 March 2022.
4. Moch H, Cubilla AL, Humphrey PA, Reuter VE, Ulbright TM. The 2016 WHO classification of tumours of the urinary system and male genital organs-part A: renal, penile, and testicular tumours. *Eur Urol*. 2016;70(1):93-105. [\[CrossRef\]](#)
5. Woodward PJ, Sohaey R, O'Donoghue MJ, Green DE. Tumors and tumor-like lesions of the testis: radiologic-pathologic correlation. *RadioGraphics*. 2002;22(1):189-216. [\[CrossRef\]](#)
6. Williamson SR, Delahunt B, Magi-Galluzzi C, et al. The World Health Organization 2016 classification of testicular germ cell tumours: a review and update from the International Society of Urological Pathology Testis Consultation Panel. *Histopathology*. 2017;70(3):335-346. [\[CrossRef\]](#)
7. Johnson JO, Mattrey RF, Phillipson J. Differentiation of seminomatous from nonseminomatous testicular tumors with MR imaging. *AJR*. 1990;154(3):539-543. [\[CrossRef\]](#)
8. Tsili AC, Tsampoulas K, Giannakopoulos X, et al. MRI in the histologic characterization of testicular neoplasms. *AJR*. 2007;189(6):W331-W337. [\[CrossRef\]](#)
9. Tsili AC, Sylakos A, Ntorkou A, et al. Apparent diffusion coefficient values and dynamic contrast enhancement patterns in differentiating seminomas from nonseminomatous testicular neoplasms. *Eur J Radiol*. 2015;84(7):1219-1226. [\[CrossRef\]](#)
10. Tsili AC, Ntorkou A, Astrakas L, et al. Diffusion-weighted magnetic resonance imaging in the characterization of testicular germ cell neoplasms: effect of ROI methods on apparent diffusion coefficient values and inter-observer variability. *Eur J Radiol*. 2017;89:1-6. [\[CrossRef\]](#)
11. Oldenburg J, Berney DM, Bokemeyer C, et al. Testicular seminoma and non-seminoma: ESMO-EURACAN Clinical Practice Guideline for diagnosis, treatment and follow-up. *Ann Oncol*. 2022;33(4):362-375. [\[CrossRef\]](#)
12. Bhatt S, Jafri SZ, Wasserman N, Dogra VS. Imaging of nonneoplastic intratesticular masses. *Diagn Interv Radiol*. 2011;17(1):52-63. [\[CrossRef\]](#)
13. Dogra VS, Gottlieb RH, Oka M, Rubens DJ. Sonography of the scrotum. *Radiology*. 2003;227(1):18-36. [\[CrossRef\]](#)
14. Mathur M, Mills I, Spektor M. Magnetic resonance imaging of the scrotum: pictorial review with ultrasound correlation. *Abdom Radiol (NY)*. 2017;42(7):1929-1955. [\[CrossRef\]](#)
15. Tsili AC, Bertolotto M, Turgut AT, et al. MRI of the scrotum: recommendations of the ESUR Scrotal and Penile Imaging Working Group. *Eur Radiol*. 2018;28(1):31-43. [\[CrossRef\]](#)
16. Kim W, Rosen MA, Langer JE, Banner MP, Siegelman ES, Ramchandani P. Us MR imaging correlation in pathologic conditions of the scrotum. *RadioGraphics*. 2007;27(5):1239-1253. [\[CrossRef\]](#)
17. Mohrs OK, Thoms H, Egner T, et al. MRI of patients with suspected scrotal or testicular lesions: diagnostic value in daily practice. *AJR*. 2012;199(3):609-615. [\[CrossRef\]](#)
18. Tsili AC, Giannakis D, Sylakos A, Ntorkou A, Sofikitis N, Argyropoulou MI. MR imaging of scrotum. *Magn Reson Imaging Clin N Am*. 2014;22(2):217-238. [\[CrossRef\]](#)
19. Manganaro L, Vinci V, Pozza C, et al. A prospective study on contrast-enhanced magnetic resonance imaging of testicular lesions: distinctive features of Leydig cell tumours. *Eur Radiol*. 2015;25(12):3586-3595. [\[CrossRef\]](#)
20. Parenti GC, Feletti F, Carnevale A, Uccelli L, Giganti M. Imaging of the scrotum: beyond sonography. *Insights Imaging*. 2018;9(2):137-148. [\[CrossRef\]](#)
21. Tsili AC, Argyropoulou MI, Giannakis D, Sofikitis N, Tsampoulas K. MRI in the characterisation and local staging of testicular neoplasms. *AJR*. 2010;194(3):682-689. [\[CrossRef\]](#)
22. Tsili AC, Argyropoulou MI, Astrakas LG, et al. Dynamic contrast-enhanced subtraction MRI for characterizing intratesticular mass lesions. *AJR*. 2013;200(3):578-585. [\[CrossRef\]](#)
23. Algebally AM, Tantawy HI, Yousef RR, Szmigielski W, Darweesh A. Advantage of adding diffusion weighted imaging to routine MRI examinations in the diagnostics of scrotal lesions. *Pol J Radiol*. 2015;80:442-449. [\[CrossRef\]](#)
24. Tsili AC, Giannakis D, Sylakos A, et al. Apparent diffusion coefficient values of normal testis and variations with age. *Asian J Androl*. 2014;16(3):493-497. [\[CrossRef\]](#)
25. Inoue C, Fujii S, Kaneda S, et al. Apparent diffusion coefficient (ADC) measurement in endometrial carcinoma: effect of region of interest methods on ADC values. *J Magn Reson Imaging*. 2014;40(1):157-161. [\[CrossRef\]](#)
26. Mukuda N, Fujii S, Inoue C, et al. Apparent diffusion coefficient (ADC) measurement in ovarian tumor: effect of region-of-interest methods on ADC values and diagnostic ability. *J Magn Reson Imaging*. 2016;43(3):720-725. [\[CrossRef\]](#)
27. Sun MR, Ngo L, Genega EM, et al. Renal cell carcinoma: dynamic contrast-enhanced MR imaging for differentiation of tumor subtypes-correlation with pathologic findings. *Radiology*. 2009;250(3):793-802. [\[CrossRef\]](#)
28. Cornelis F, Tricaud E, Lasserre AS, et al. Routinely performed multiparametric magnetic resonance imaging helps to differentiate common subtypes of renal tumors. *Eur Radiol*. 2014;24(5):1068-1080. [\[CrossRef\]](#)
29. Ohno Y, Hatabu H, Takenaka D, et al. Dynamic MR imaging: value of differentiating subtypes of peripheral small adenocarcinoma of the lung. *Eur J Radiol*. 2004;52(2):144-150. [\[CrossRef\]](#)
30. Turkbey B, Kobayashi H, Ogawa M, Bernardo M, Choyke PL. Imaging of tumor angiogenesis: functional or targeted? *AJR*. 2009;193(2):304-313. [\[CrossRef\]](#)
31. Oto A, Yang C, Kayhan A, et al. Diffusion weighted and dynamic contrast-enhanced MRI of prostate cancer: correlation of quantitative MR parameters with Gleason score and tumor angiogenesis. *AJR*. 2011;197(6):1382-1390. [\[CrossRef\]](#)
32. Tuncbilek N, Kaplan M, Altaner S, et al. Value of dynamic contrast-enhanced MRI and correlation with tumor angiogenesis in bladder cancer. *AJR*. 2009;192(4):949-955. [\[CrossRef\]](#)

Spontaneous Intracystic and Subdural Hemorrhage of an Arachnoid Cyst: A Case Report with Baseline Imaging of an Intact Cyst

Muhsin Özgün Öztürk¹, Zeynep Betül Deve¹

Department of Radiology, Erzincan University, School of Medicine, Erzincan, Turkey

Cite this article as: Öztürk MÖ, Deve ZB. Spontaneous intracystic and subdural hemorrhage of an arachnoid cyst: A case report with baseline imaging of an intact cyst. *Current Research in MRI* 2023;2(3):70-71.

Corresponding author: Muhsin Özgün Öztürk, e-mail: ozturk_bul@hotmail.com

Received: October 12, 2023 **Accepted:** October 23, 2023 **Publication Date:** November 17, 2023

DOI:10.5152/CurrResMRI.2023.23081



Content of this journal is licensed under a Creative Commons Attribution-NonCommercial 4.0 International License.

Dear Editor,

I hope this letter finds you well. I am writing to present to you a recent medical event that we have encountered and found significant. This case involves a rare intracranial hemorrhage associated with an arachnoid cyst (AC).

Arachnoid cysts are benign fluid accumulations that develop between the inner and outer layers of the arachnoid in the cerebrospinal axis.¹ They usually form during childhood and are often detected incidentally.² However, approximately 5% of cases can lead to symptoms, including headaches, dizziness, vomiting, cognitive impairment, and, rarely, sensory-motor symptoms.³ On rare occasions, these cysts can become complicated, resulting in intracystic and/or subdural hemorrhages.¹⁻⁵

In this letter, we present the case of a 70-year-old male patient who experienced a rare event. The patient's history revealed the presence of a Galassi type 3 AC, measuring $7 \times 5 \times 5$ cm, in the left middle cranial fossa on computerized tomography (CT) and magnetic resonance imaging conducted within the past year (Figure 1, 2). This cyst triggered a spontaneous intracystic subacute hemorrhage, which subsequently led to an associated subacute subdural hematoma and the patient's current symptoms. The patient had no history of trauma at the time of presentation. Following a cranial CT scan, a 39-mm-thick subacute subdural hematoma was detected in the left frontotemporoparietal extra-axial

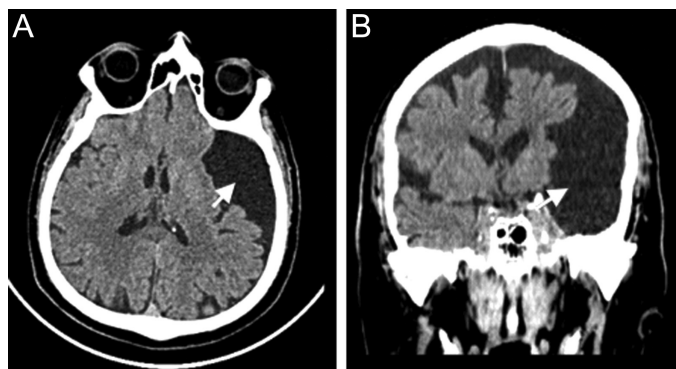


Figure 1. Computed tomography images of the patient a year ago: (A) Axial computed tomography: left-sided incidental $7 \times 5 \times 5$ cm Galassi type 3 arachnoid cyst (white arrow). (B) Coronal computed tomography: incidental left-sided $7 \times 5 \times 5$ cm Galassi type 3 arachnoid cyst (white arrow) displaces temporal lobes significantly and parietal and frontal lobes mildly.

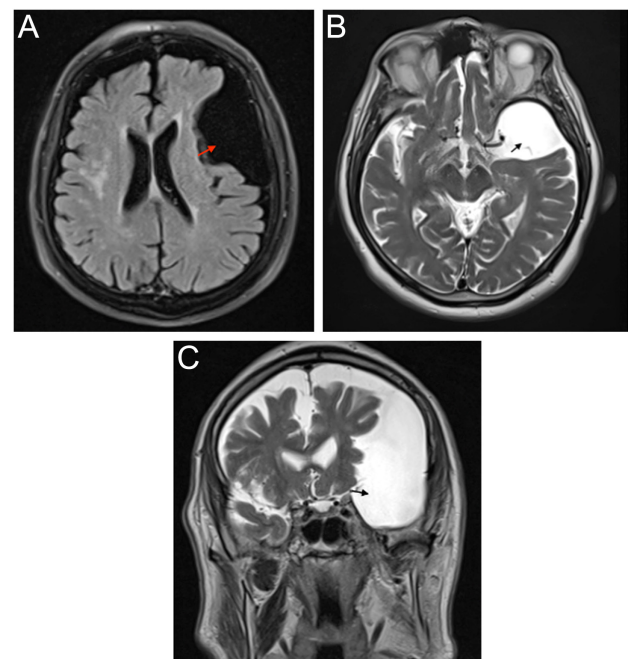


Figure 2. Magnetic resonance images of the patient a year ago: (A) Axial Fluid attenuated inversion recovery (FLAIR): left-sided intracranial Galassi type 3 arachnoid cyst (red arrow). (B) Axial T2-weighted magnetic resonance imaging: left-sided intracranial Galassi type 3 arachnoid cyst (black arrow). (C) T2-weighted coronal magnetic resonance imaging: left-sided intracranial Galassi type 3 arachnoid cyst (black arrow), which displaces temporal lobes significantly and parietal and frontal lobes mildly.

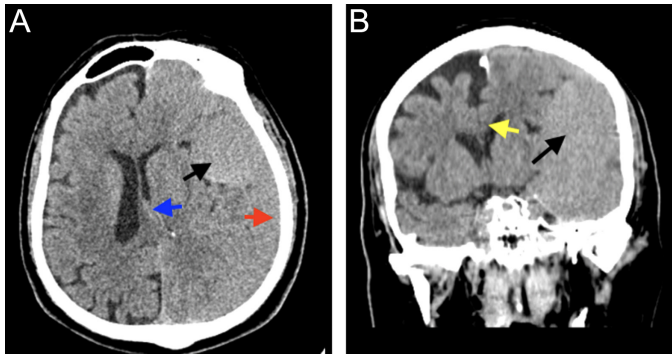


Figure 3. Computed tomography images at the time of admission: (A) Axial computed tomography: subacute subdural hemorrhage (red arrow) and accompanying intracystic subacute hemorrhage (black arrow), right-sided shift of midline structures (blue arrow) (B) Coronal computed tomography: subfalcian herniation to the right (yellow arrow) and accompanying intracystic subacute hemorrhage (black arrow).

space (Figure 3). Furthermore, the intracystic fluid within the AC appeared isodense compared to gray matter.

Considering the rapid progression of the patient's symptoms and the displacement of brain structures, a burrhole craniostomy was performed on the same day. A follow-up CT scan conducted 2 days later did not reveal any acute/subacute bleeding, but moderate subdural effusion was observed (Figure 4).

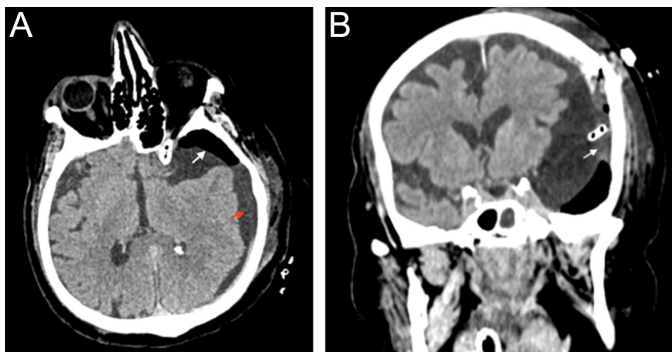


Figure 4. Postoperative computed tomography images after burrhole craniostomy: (A) Axial computed tomography: moderate subdural hypodense collection (red arrow) and post-operative extra-axial pneumocephalus (white arrow). (B) Coronal computed tomography: The border of arachnoid cyst adjacent to the subdural collection (white arrow).

According to recent reports, only 57 cases of spontaneous rupture and 32 cases of spontaneous intracystic hemorrhage have been documented in the literature, and around half of the patients with spontaneous intracystic hemorrhage were in childhood.^{2,3} Spontaneous subacute or acute intracystic hemorrhage with an imaging study prior to the hemorrhagic event is exceptionally rare, with only a few cases.¹

This case highlights a rare complication of ACs and underscores the importance of prompt medical intervention. Given the potential for spontaneous rupture of blood vessels within and around the cyst, patients with such cysts must be evaluated and treated promptly.³ In this case, having access to the patient's previous imaging allowed for a rapid diagnosis and, consequently, prompt treatment.

In conclusion, this rare case presentation aims to raise awareness regarding spontaneous intracystic and subdural hemorrhages associated with ACs and to encourage further research in the diagnosis and treatment of such cases.

Informed Consent: Written informed consent was obtained from patient who participated in this study.

Peer-review: Externally peer-reviewed.

Author Contributions: Concept – M.Ö.Ö.; Design – M.Ö.Ö., Z.B.D.; Supervision – M.Ö.Ö.; Resources – M.Ö.Ö.; Materials – M.Ö.Ö., Z.B.D.; Data Collection and/or Processing – M.Ö.Ö.; Analysis and/or Interpretation – M.Ö.Ö.; Literature Search – M.Ö.Ö., Z.B.D.; Writing Manuscript – M.Ö.Ö., Z.B.D.; Critical Review – M.Ö.Ö.

Declaration of Interests: The authors declare that they have no competing interest.

Funding: The authors declared that this study has received no financial support.

REFERENCES

- Kim D, Yoo D. Intracystic hemorrhage of an arachnoid cyst: a case with prediagnostic imaging of an intact cyst. *Investig Magn Reson Imaging*. 2021;25(1):43-46. [\[CrossRef\]](#)
- Ferreira TSH, Malveira LRC, Neto AG. Spontaneous subdural and intracavitary hemorrhage of temporal arachnoid cyst in an adult patient. *Interdisciplinary Neurosurgery*. 2021;23:100830. [\[CrossRef\]](#)
- Leavitt LA, Nanda P, Stemmer-Rachamimov A, Dunn GP, Jones PS. Spontaneous rupture of an arachnoid cyst in an adult: illustrative case. *J Neurosurg Case Lessons*. 2023;5(7):CASE22420. [\[CrossRef\]](#)
- Joel P, Anand K, Rami O A. Spontaneous intracystic hemorrhage in an adult with cerebellopontine angle arachnoid cyst and management: A case report. *Neurosurg Cases Rev*. 2021;4(2):070. [\[CrossRef\]](#)
- Liu B, Wang C, Qu Y. Treatment of arachnoid cyst with spontaneous hemorrhage with atorvastatin. *Front Pharmacol*. 2019;10:1343. [\[CrossRef\]](#)

Acknowledgement of Reviewers

The Editorial Board gratefully appreciates the assistance of all our reviewers listed below to acknowledge their considerable insights and input for the Current Research in MRI in 2023.

To get acknowledgment form please visit the online manuscript system.

Ahmet Gürkan Erdemir
Barış Özöner
Barış İrgül
Behiç Akyüz
Berna Uçan
Bünyamin Ece
Çiğdem Üner
Düzgün Can Şenbil
Eda Beykoz Çetin
Emre Mircik
Erdal Karavas
Erdem Fatihoğlu

Fatma Dilek Gökharman
Ferhat Can Pişkin
Gamze Durhan
Gökçe Çınar
Gunjan Jindal
Hasan Yiğit
Hüseyin Akkaya
İbrahim Feyyaz Naldemir
Kristian Nikolaus Schneider
Leyla Karaca
Mehmet Coşkun
Melahat Kul

Mesut Furkan Yazar
Mustafa Koyun
Nüket Nermin Göçmen Karabekir
Oğuzhan Tokur
Okan Dilek
Ömer Kazcı
Özlem Aydın
Özlem Kadirjan
Özge Aslan
Pankaj Singh
Taner Kösetürk
Volkan Kızılgöz